ABSTRACT

MICROACCELEROMETER WITH MECHANICALLY-LATCHED MEMORY

by
Zhenyu Ma

A new mechanically-latching micromachined accelerometer is designed in this thesis based on the large deflection of a microcantilever beam. This surface micromachined device moves in the plane of the substrate surface. This device is surface micromachined with no backside etching needed. The interaction of the friction tether and the dimensions of the cantilever beam have been modeled and calculated. The design acceleration sensitivity range is from 100G to 1000G. The photomask set has been designed by using the Mentor Graphics system. The dimension of individual accelerometers ranges from 100 to 1000 micrometers in length to tens of micrometers in width. A special prototype mask containing 8 latched microaccelerometers has been designed with 3 levels and an overall dimension of 5*5 mm. Fabrication techniques for this accelerometer are described. This proposed cantilever beam is to be fabricated by low pressure chemical vapor deposition. A test station for creating a controlled acceleration has been designed and constructed. The test acceleration can be created in the range from 0 to 200G.

MICROACCELEROMETER WITH MECHANICALLY-LATCHED MEMORY

by
Zhenyu Ma

A Thesis
Submitted to the Faculty of
New Jersey Institute of Technology
in Partial Fulfillment of the Requirements for the Degree of
Master of Science in Applied Physics

Department of Physics

January 1995

Blank Page

APPROVAL PAGE

MICROACCELEROMETER WITH MECHANICALLY-LATCHED MEMORY

Zhenyu Ma

Dr. William N. Carr, Thesis Advisor   Date
Professor and Holder of Sponsored Chair in Microelectronics, NJIT

Dr. Nuggehalli M. Ravindra, Committee Member   Date
Associate Professor of Physics, NJIT

Dr. Kenneth R. Farmer, Committee Member   Date
Assistant Professor of Physics, NJIT

BIOGRAPHICAL SKETCH

Author: Zhenyu Ma

Degree: Master of Science in Applied Physics

Date: January 1995

Undergraduate and Graduate Education

- Master of Science in Applied Physics,
  New Jersey Institute of Technology,
  Newark, New Jersey, 1995

- Bachelor of Science in Materials Science and Engineering,
  Tsinghua University, Beijing, P.R.China, 1990

Major: Applied Physics

Presentations and Publications:

Z. Ma, Q. Wang, Y. Zan, Y. Yu and L. Lin, "Determination of Interstitial Oxygen Concentration in Heavily Doped Silicon by Combination of Neutron Irradiation and FTIR," *Chinese Journal of Semiconductors*, Vol. 15, pp.217-221, March, 1994.

This thesis is dedicated to
my wife and my parents

ACKNOWLEDGMENT

TABLE OF CONTENTS

Chapter	Page

TABLE OF CONTENTS
(Continued)

LIST OF TABLES

LIST OF FIGURES

LIST OF FIGURES
(Continued)

CHAPTER 1

INTRODUCTION

1.1 Introduction

The measurement of acceleration is a physical quantity gaining increasing interest in many systems for monitoring, control or measurement applications. Recently, many new micro designs of accelerometers manufactured utilizing silicon micromachining technology have been reported [1][2]. This is because the semiconductor silicon makes extreme size and weight reduction possible, together with a low cost and compatibility with silicon integrated-circuit(IC) fabrication. Advances in silicon micromachining have permitted the convenient fabrication of compact structures providing new microsensors and opening up new application areas.

For example, microaccelerometers are already being used on some kinds of vehicles for active suspension systems and passive restraints. These devices now are being designed into new vehicle models to be introduced over the next few years. Consequently the market for automotive accelerometers will increase rapidly. By the end of this century as many as 35 000 000 units microaccelerometer will be required per year if each vehicle only contains a single accelerometer.

The initial smaller markets are being met by a variety of technologies. As the markets increase in size, it is anticipated that the technologies suitable to higher volume production (especially micromachined silicon sensors) will dominate.

The first silicon microaccelerometer was reported by Roylance and Angell in 1979 [3]. Since then, many different approaches have been used to fabricate these devices. Silicon accelerometers have been successfully produced using bulk machining [4][5], surface micromachining [6][7][8][9], dissolved wafer micromachining [10], and wafer bonding [11], of these fabrication techniques, the last three constitute a

1

class of structures called microaccelerometers. Microaccelerometers have potential advantages of lower cost, higher sensitivity, reduced weight, and smaller size compared to other accelerometers.

1.2 Previous Work

The forces arising from acceleration can be determined by direct measurement of the force or by inferring it from the displacement of a suspended mass or the stress/strain in the spring mounting. These concepts have been embodied in previous microaccelerometer designs.

1.2.1 Piezoresistive Accelerometers

Silicon exhibits the piezoresistive effect, can be chemically etching defined with great precision, is very strong and is mechanically stable, and the conditioning electronics can be integrated on the sensor substrate. Pizoresistance can be used to measure the stress on a seismic mass that is cause by acceleration.

Piezoresistive accelerometers are normally either of single-ended cantilever or of double-ended bridge design. The former have the advantage that a smaller area of silicon is used to achieve a given sensitivity. The latter use several piezoresistors with a bridge design where the silicon mass is support by two or more support beams. Schematic representations of each type are given in Figure 1.1(a, b). The main disadvantages of piezoresistive accelerometers are that characteristics are quite temperature sensitive. They are also very sensitive to mounting and other induced stresses.

1.2.2 Capacitive Silicon Accelerometer [12]

The capacitive accelerometer has the advantage of higher mechanical stability, lower temperature coefficients, higher mechanical overload resistance and higher sensitivity

and resolution. The disadvantage is that electromagnetic interference is a problem and the readout can be more complex. Figure 1.2 shows an accelerometer using capacitive design.
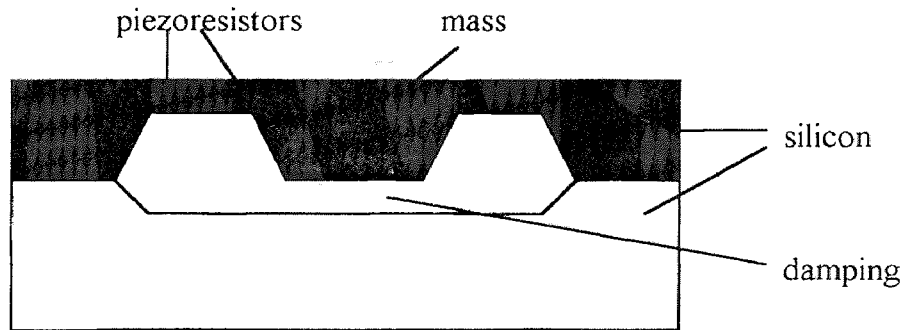
(a)
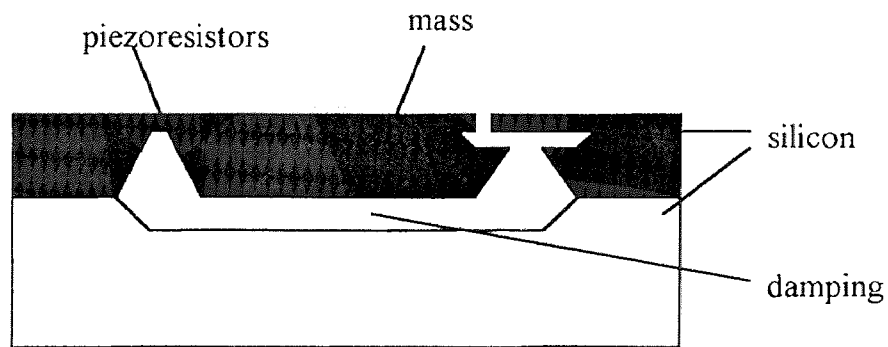
(b)

Figure 1.1 (a) (b) Microaccelerometer with piezoresistor transducer
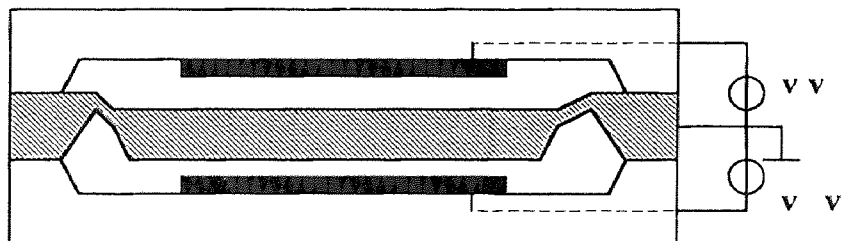
Figure 1.2 Microaccelerometer with capacitance readout
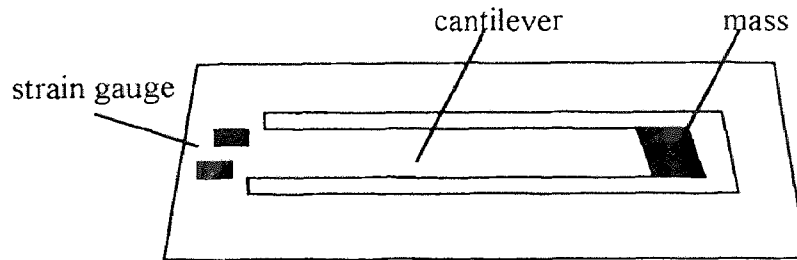
Figure 1.3 Microaccelerometer with the film strain gauge readout

1.2.3 Thick-Film Strain Gauge Accelerometer [13]

Sensors exploiting the substantial strain sensitivity of certain thick-film resistor inks can be produced at very low cost in both medium and large production volumes. Figure 1.3 outlines one possible cantilever accelerometer design. The main problem here is that standard substrate materials are very stiff. It is difficult to design a structure which offers high strains (high sensitivity) and at the same time achieves both a reasonable robustness and acceptable bandwidth.

1.2.4 Force Balance Accelerometer [14]

In this microaccelerometer, an electromagnetic or electrostatic force is generated which opposes the acceleration forces. Thus the mass maintains an equilibrium position. The energy required is a measure of the applied acceleration. In general, force balance devices offer good performance because a wide bandwidth and high sensitivity can be achieved, but normally they are more complex and expensive than other non-feedback methods. This is a nulling -type device which provides superior immunity to nonlinearties.

1.2.5 Micromachined Resonators [15]

When the tension in a guitar string is changed, there is a corresponding change in the

resonant frequencies which create its characteristic timbre. Similarly the resonant frequency is also changed in a microbeam or microcantilever device. The resonator becomes a stress sensitive element capable of detecting acceleration forces. The output is in the pseudo-digital form of a frequency. The bridge structure is shown in Figure 1.4.
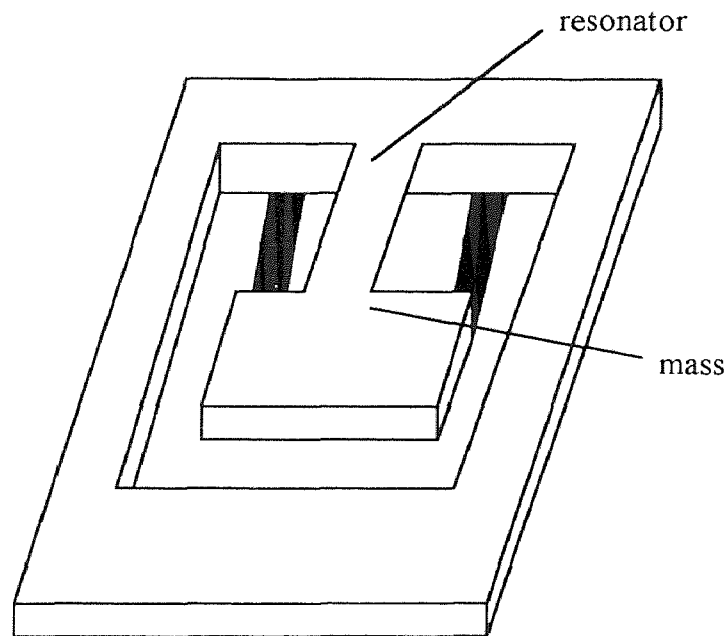
Figure 1.4 Microaccelerometer with resonant beam

The structure can be fabricated by the micromachining of silicon. The excitation is normally electrostatic, photothermal, or electrothermal. A very high resolution can be achieved in each device. The thermal excitation can cause undesirable thermal stresses.

1.2.6 Mechanically-latching Micromachined Accelerometer

Ciarlo [16] has used the anisotropic etching of bulk silicon wafers to fabricate a latching accelerometer shown in Figure 1.5 (a). It consists of two separate cantilever

beams in the plane of the silicon substrate with silicon proof masses on their free ends. The accelerometer is designed so that when it experiences an acceleration in the upward direction, the horizontal cantilever will deflect downward and push the vertical cantilever to the left. If the acceleration is above a certain threshold value, the two released cantilevers will latch as shown in Figure 1.5 (b). In this thesis the author uses the surface of the silicon wafer to fabricate mechanically-latching accelerometers without bulk micromaching. The basic idea is discussed in section 1.3.

(a)   (b)
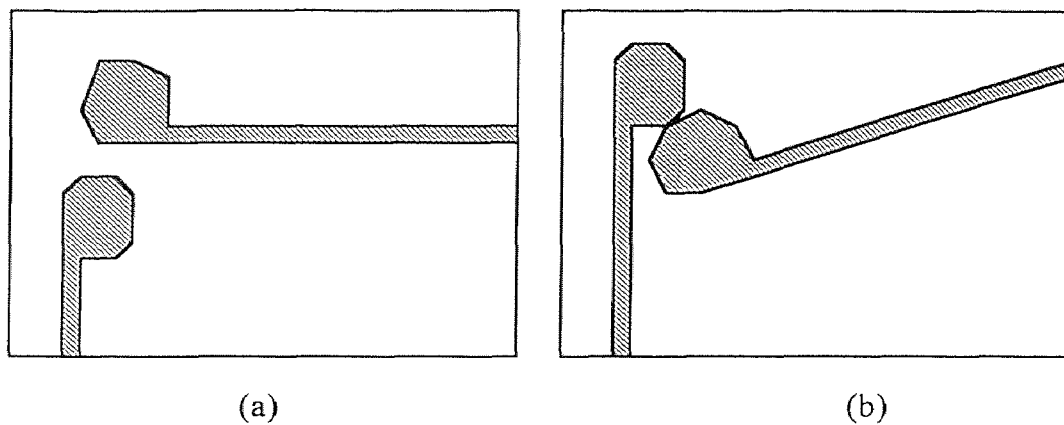
Figure 1.5 (a) (b) Illustration of the Ciarlo bulk microaccelerometer (a) the unlatched position (b) latched position

1.3 The Mechanical-Latching Accelerometer of This Thesis

The structure in section 1.2.5 is mainly moved vertically related to the wafer surface. In this thesis the author uses the silicon micromaching process to fabricate the structure of accelerometer which moves within the plane of the device top surface. Etching from backside of wafer to release space for the accelerometer to move is unnecessary. The accelerometer of this thesis has its own unique features including ease of fabrication and low cost.

The test structure is shown in Figure 1.6 with 8 microaccelerometers included.

One side of the mass is connected to a cantilever beam and a support pedestal, the other side is a pointer. The basic idea is that when the mass is accelerated a force causes it to move, when the force of acceleration is balanced by the force generated by cantilever beam deflection, it stops and the pointer points to the scale on the friction tether. Then we can know the angle of the deflection. Using the model for large deflection of the cantilever beam, the relation of the angle as a function of acceleration is determined. In this thesis eight different devices with different parameters on one support pedestal are designed. Advantages of this design concept include saving space and testability.
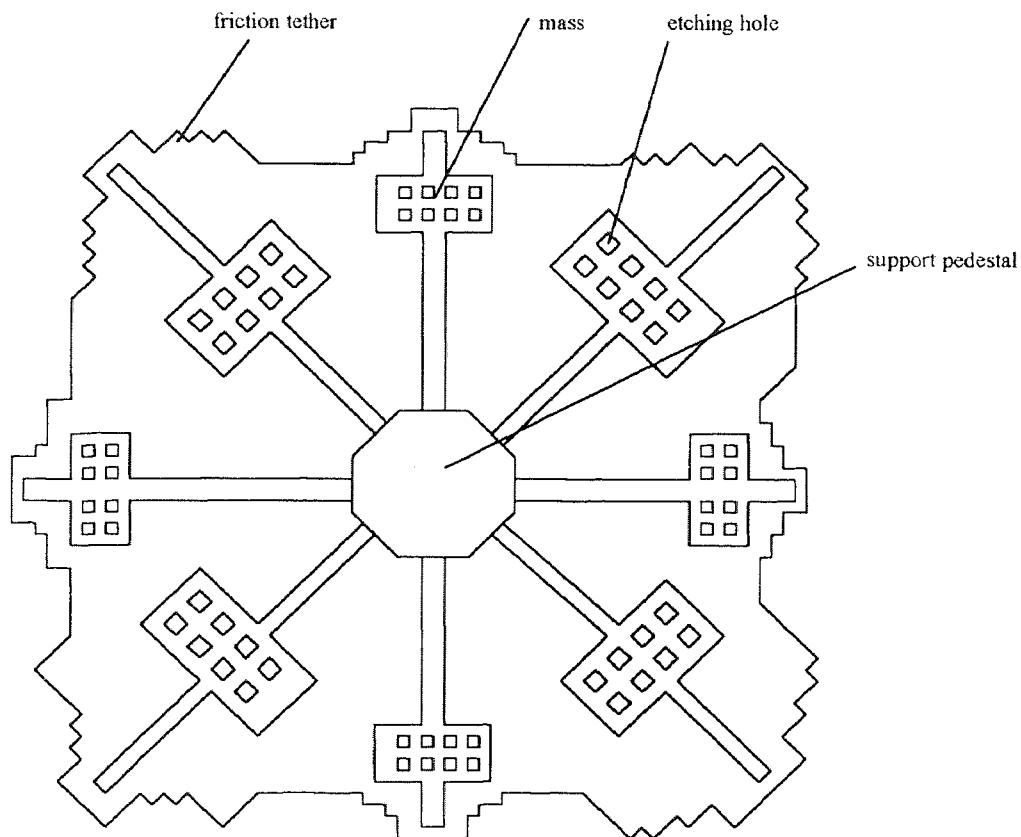
Figure 1.6 Schematic top view of mechanical-latching accelerometer with cantilever polysilicon mass structure

1.4 Thesis Goal

This thesis is separated to six chapters.

In chapter 1, previous work and basic concepts of my mechanical-latching accelerometer are discussed.

In chapter 2, by using the model of large deflection of cantilever beam, the optimize parameter of the cantilever beam and the coordinates of deflected tip neglecting friction are calculated.

In chapter 3, three-layer physical database masks are created by using Mentor Graphics VLSI design system.

In chapter 4, the fabrication processing conditions and processing steps are discussed.

In chapter 5, the experimental circuit to generate the required acceleration for testing is established

In chapter 6, the final conclusions about my thesis are included. Some suggestions for future improving mechanically-latched accelerometer are made.

CHAPTER 2

ACCELEROMETER DEVICE MODELING AND DESIGN

2.1 Properties of Polycrystalline Silicon

Polycrystalline films of silicon are being used in an increasing number of sensor applications. Polysilicon is attractive because its deposition and processing technologies have been well developed for integrated-circuit applications and also because its compatibility with silicon integrated circuits. For example, diaphragms are used in pressure sensors, cantilever beams are used in accelerometers and resonant-beam sensors.

Polycrystalline silicon permits a variety of sensor applications in which stress and other mechanical effects can dominate the device behavior. Characteristics of polysilicon can be significantly affected by the grain boundaries as well as by the differently oriented crystallites in the film, and this requires very carefully controlled chemical vapor deposition techniques.

In sensor applications, the mechanical properties, and therefore the structure of the polysilicon films are even more critical. In cantilever beams, the mechanical properties should be uniform through the thickness of the polysilicon layer so that the beam is not deflected until an external force is applied. H. Guckel [17] calculated the mechanical properties of polysilicon film from the properties of single crystal silicon by taking into account the effect of the film morphology. In single crystal material, Young's modulus, the Poisson ratio and the shear modulus are calculated using the compliance coefficients and appropriate tensor transformations [18,19]. Calculations of the properties for polycrystalline material require averaging over the various grain orientations and distribution. A texture function $G(\Phi,\theta)$ is defined to describe the film

morphology in his work. Young's modulus for polysilicon is calculated from the following integral:

$$<E>=(1/4\pi)\iint G(\Phi,\theta)(1/s_{33}')d\Phi d\theta \qquad (2.1)$$

where Φ and θ are the Eulerian angles for coordinate transformations, s_{33}' is the effective compliance coefficient in the x_3' direction for single crystal material. Integration in Equation 2.1 is performed over all possible crystal orientations. The effect of grain boundaries is neglected in this formulation.

Young's modulus, the Poisson ratio and the shear modulus calculated by H.Guckel et al [16] for polysilicon using Equation 2.1 and values are given in Table 2.1. The value of Young's modulus is also used in my calculation for the determination of accelerometer physical dimensions.

Table 2.1 Calculated Values and Temperature Coefficients for polysilicon

Property	Value	TC (ppm/°c)
Young's modulus E	161G Pa	-74.5
Poisson's Ratio ν	0.226	+25.7
Shear Modulus G	65.9GPa	-78.5
Bulk Modulus B	97.8GPa	-53.2
Tensile breaking stress σ_{max}	$2.2*10^5 N/m^2$	
Tensile breaking strain ε_{max}	2.6%	

2.2 The Model of Large Deflection of Cantilever Beam

To find the internal stress distribution produced by pure bending (Figure 2.1), the deformation of the beam must be considered [20]. We will assume that the xy plane contains the loads. Hence the bending deflections will take place in the xy plane also. Under the action of the bending moments M, the axis of the beam is bent into a circular arc (Figure 2.1). Cross sections of the beam, such as mn and pq, remain plane and normal to the longitudinal fibers of the beam. The fact that cross sections of a beam in pure bending remain plane can be established experimentally by making careful strain measurements, or it can be established on a purely theoretical basis. In the latter instance, it is necessary only to observe that all elements of the beam deform identically, which is possible only if the cross sections remain plane. This conclusion is valid irrespective of whether the material of the beam is linearly elastic or not.
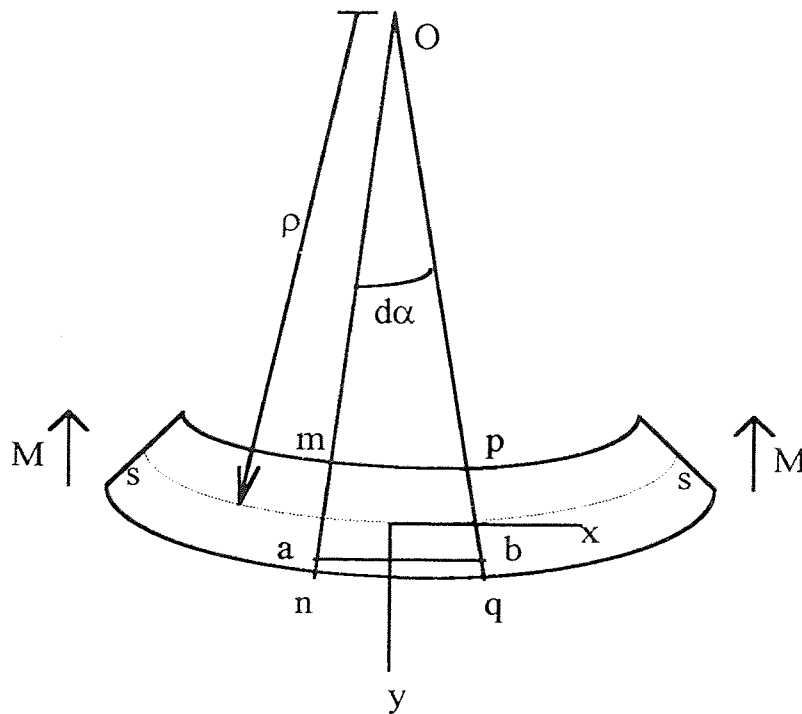
Figure 2.1 Deformation of a beam in pure bending

As a result of the bending deformations shown in Figure 2.1, we find that the cross sections mn and pq rotate with respect to each other about axes perpendicular to the xy plane, so that convex side of the beam is elongated while the concave side is shortened. Thus, the upper part of the beam is in compression while the lower beam is in tension. Somewhere between the top and bottom of the beam there is a surface in which the longitudinal fibers do not change in length. This surface, indicated by the dashed line ss in Figure 2.1, is called the neutral surface of the beam. Its intersection with any cross-sectional plane is called the neutral axis of the cross section. After deformation, the planes of two adjacent cross sections mn and pq intersect at point O, which is the center of curvature for the longitudinal axis of the beam. The angle between these planes is denoted by $d\alpha$, and the radius of curvature is denoted by ρ. From the geometry of the figure we see that

$$\kappa = \frac{1}{\rho} = \frac{d\alpha}{ds} \qquad (2.2)$$

where κ is the curvature, equal to the reciprocal of the radius of curvature, and ds is the length of the element between the two adjacent cross sections mn and pq.

The elongation of a typical longitudinal fiber ab, distance y from the neutral surface, can be found as follows. The total length of the fiber is $(\rho+y)d\alpha$, Inasmuch as the original length of the fiber was ds, we see that its elongation is ds/ρ and the corresponding strain ε_x is

$$\varepsilon_x = \frac{y}{\rho} = \kappa y \qquad (2.3)$$

This equation shows that the longitudinal strain ε_x is directly proportional to the curvature and to the distance y from the neutral surface ss. When the structure under consideration is below the neutral surface ss, the distance y is positive and the strain is positive(tension). When the fiber is above the neutral surface, both y and ε_x will be negative, indicating that the material is in compression. This equation is valid when the material of the beam has any type of stress-strain diagram.

For a beam constructed of an elastic material with a linear stress-strain diagram, we have $\sigma = E\varepsilon$. Therefore, the normal stress σ_x in the beam by using Equation 2.3 is

$$\sigma_x = \kappa E y \tag{2.4}$$

One notes that σ_x varies linearly with the distance y from the neutral axis, as shown in Figure 2.2. There are tensile stresses below the neutral axis and compressive stresses above. The resultant of these stresses must be identical to the bending couple M acting on the cross section.
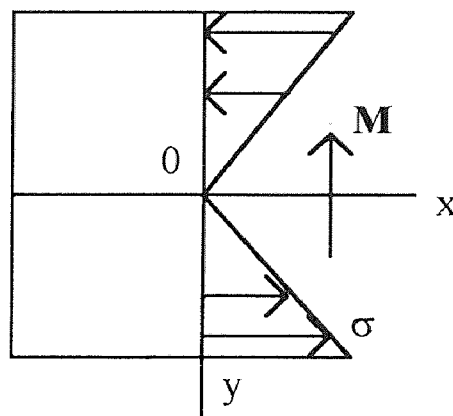
Figure 2.2 Stress distribution in a beam

The moment of the elemental force $\sigma_x dA$ about the neutral axis is $\sigma_x y dA$. The integral of all such elemental moments over the entire cross-sectional area must equal the bending moment M; thus

$$M = \int \sigma_x y dA = \kappa E \int y^2 dA = \kappa EI \qquad (2.5)$$

where I is the moment of inertia

$$I = \int y^2 dA \qquad (2.6)$$

Equation 2.5 can be rewritten in the form

$$\kappa = \frac{1}{\rho} = \frac{M}{EI} \qquad (2.7)$$

The Equation 2.7 can be rewritten as Equation 2.8, and Equation 2.8 is for the simulation assuming large deflections of the cantilever beams [20]:

$$EI\frac{d\theta}{ds} = -M \qquad (2.8)$$

The quantity $d\theta/ds$ represents the curvature of the beam that is the rate of change of θ (the angle of rotation of the end of the cantilever curve) with respect to s (the distance measured along the cantilever itself).

Let us consider the cantilever beam AB shown in Figure 2.3, the load P is assumed to produce large deflections of the beam, resulting in the end of the beam, moving from point B to B'. The angle of rotation of the end of the beam is

denoted by θ, and the horizontal and vertical displacements are δ_x and δ_y, respectively. The length AB' of the deflection curve is equal to the initial length because axial changes in length due to direct tension are neglected. Because the beam is statically determinate, the expression for the bending moment M can be obtained easily and substituted into Equation 2.8. After considerable manipulation of the equation, including a change of the dependent variable, and also after applying the appropriate boundary conditions, the solution of the equation can be obtained in terms of elliptic functions. The detail deduction is in R. F. Fay and some other references [21][22][23][24]. Equations for finding θ, δ_x and δ_y are presented below. Specifically, the transcendental equation for finding the angle θ is the following:
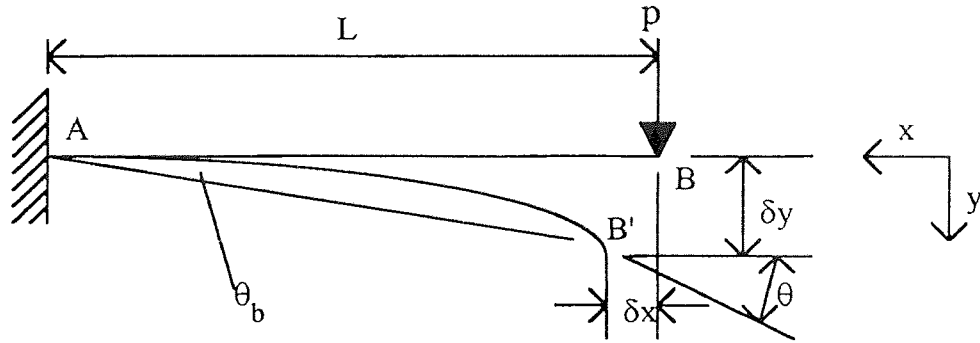
Figure 2.3 Large deflections of a cantilever beam

$$F(k) - F(k,\phi) = \sqrt{\frac{PL^2}{EI}}$$ (2.9)

where F(k) = complete elliptic integral of the first kind

$$= \int_0^{\frac{\pi}{2}} \frac{dt}{\sqrt{1 - k^2 \sin^2 t}}$$ (2.10)

where $F(k,\phi)$ = elliptic integral of the first kind

$$= \int_0^\phi \frac{dt}{\sqrt{1-k^2\sin^2 t}} \tag{2.11}$$

where

$$k = \sqrt{\frac{1+\sin\theta}{2}} \tag{2.12}$$

$$\phi = \arcsin\frac{1}{k\sqrt{2}} \tag{2.13}$$

and P is the force added at the end of the cantilever beam. We can obtain numerical values of elliptic integrals $F(k)$ and $F(k,\phi)$ by using handbooks [25]. The calculation procedure is as follows:

(1) Assume a value of θ.

(2) calculate k from Eq.(2.12).

(3) obtain the corresponding value of $F(k)$ from a table of elliptic functions

(4) calculate ϕ from Eq.(2.13)

(5) knowing k and ϕ, obtain the value of $F(k,\phi)$ from a table

(6) calculate the load P from Equation 2.9, this process will give the load P that corresponds to the particular assumed value of θ.

(7) because $tg\theta_b = \frac{\delta_y}{L-\delta_x}$, so combined with Equation (2.30)(2.35), the relation between θ_b and P can be gotten.

(8) finally from $P = m*a$, we can express

$$tg\theta_b = \frac{L - \sqrt{\frac{4EI}{ma}}(E(k)-E(k,\phi))}{\sqrt{\frac{2EI\sin\theta}{ma}}} \tag{2.14}$$

2.3 Angle Deflection Calculation Neglecting Friction

Figure 2.4, 2.5 shows the design of mechanically-latched accelerometer. The next step is to determine the dimension of the design. By using the equation and calculation procedure above, we get the relation between θ, θ_b, P and F(k)-F(k,ϕ) in table 2.2, 2.3.
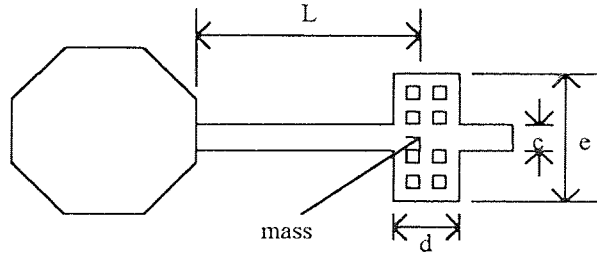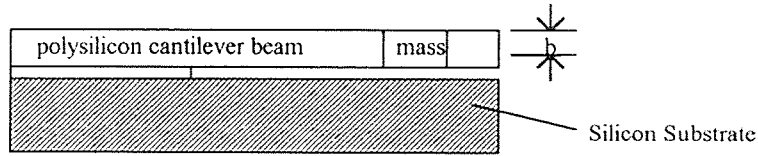

Figure 2.4 Top view of cantilever beam

Figure 2.5 Side view of cantilever beam

Then using Equation 2.14

$$tg\theta_b = \frac{L - \sqrt{\dfrac{4EI}{ma}}(E(k)-E(k,\phi))}{\sqrt{\dfrac{2EI\sin\theta}{ma}}}$$

get the relation of θ_b and acceleration a. The result is shown in figures 2.6-2.8

Young's modulus $E_{polysilicon}$ is 161GPa,

and $\qquad I=\dfrac{bc^3}{12}$ $\qquad\qquad\qquad$ (2.15)

$m=d*e*b*2.33g/cm^3$ (the weight of cantilever beam itself has been omitted because it is small compare to the mass)

The number of b, c, L, d, e can be chosen to find optimized dimension.

In this simulation I choose:

b is the thickness of cantilever beam (b=3μm)

c is the width of cantilever beam (c=2μm, 5μm, 10μm)

L is the length of cantilever beam (L=250μm, 500μm, 1000μm)

Table 2.2 The relation of θ and F(k)-F(k,φ)

θ	k	φ	$F(k)$ $\int_0^{\frac{\pi}{2}}\dfrac{dt}{\sqrt{1-k^2\sin^2 t}}$	$F(k,\phi)$ $\int_0^{\phi}\dfrac{dt}{\sqrt{1-k^2\sin^2 t}}$	F(k)-F(k,φ)
----	------	-----	------	------	------
0°	0.7071	90	1.8541	1.8541	0
5°	0.7373	73.55	1.9356	1.5087	0.4269
10°	0.7660	67.38	1.9341	1.3321	0.6040
15°	0.7934	63.04	2.0339	1.2633	0.7706
20°	0.8192	59.68	2.0843	1.1879	0.8964
25°	0.8434	56.97	2.1565	1.1349	1.0216
30°	0.8660	54.74	2.2064	1.0849	1.1215
35°	0.8870	52.86	2.2568	1.0359	1.2209
40°	0.9063	51.28	2.3088	1.0010	1.3078
45°	0.9239	50	2.5074	0.9876	1.5198

Table 2.3 The relation of θ and $θ_b$

$θ_b$	0°	5°	10°	15°	20°	25°	30°	35°	40°	45°
θ	0°	4.04°	7.93°	13.24°	16.6°	19.9°	22.6°	25°	27.1°	34.1°

d*e*b is the volume of the mass (d=100μm, e=100μm)

a is the normal acceleration magnitude added on cantilever beam

In these graphs, the unit of acceleration is G=9.8m/s², the unit of angle θ is degree, the dimension of the mass is same in the three graphs(d=100μm, e=100μm).
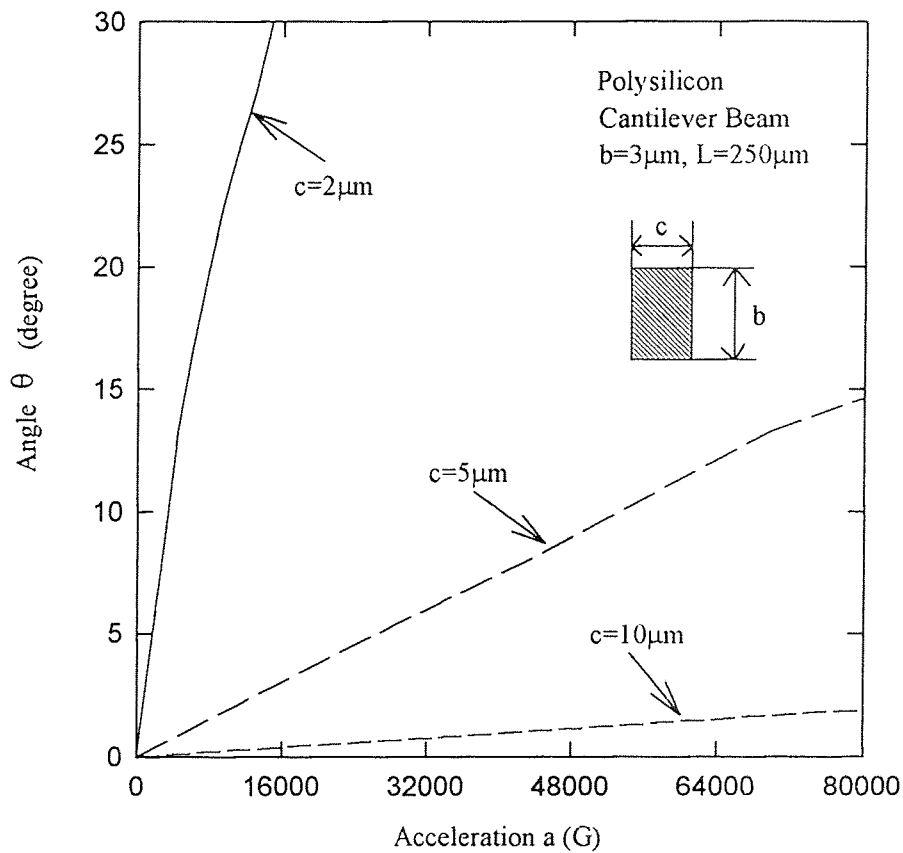

Figure 2.6 The relation of acceleration and deflection angle neglecting friction (L=250μm)
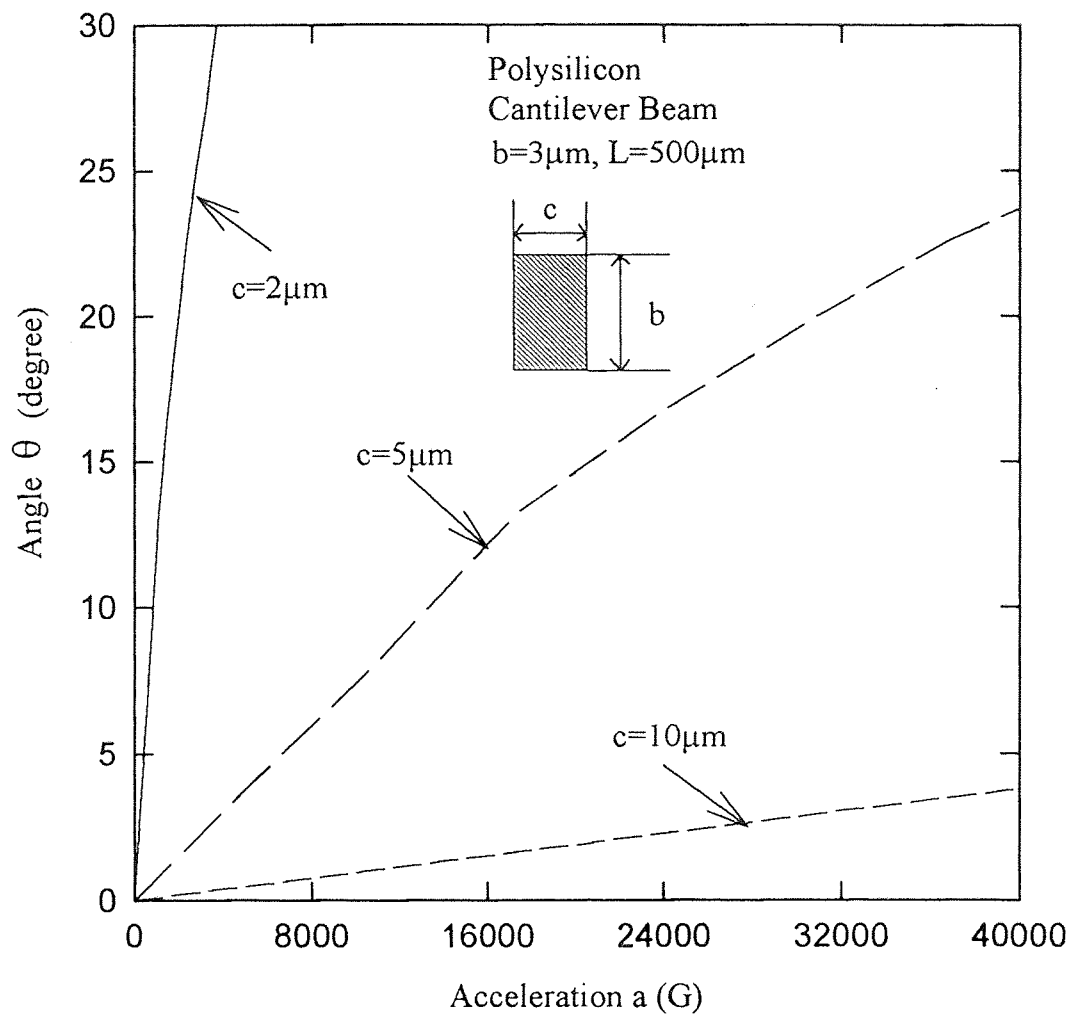
Figure 2.7 The relation of acceleration and deflection angle neglecting friction (L=500μm)
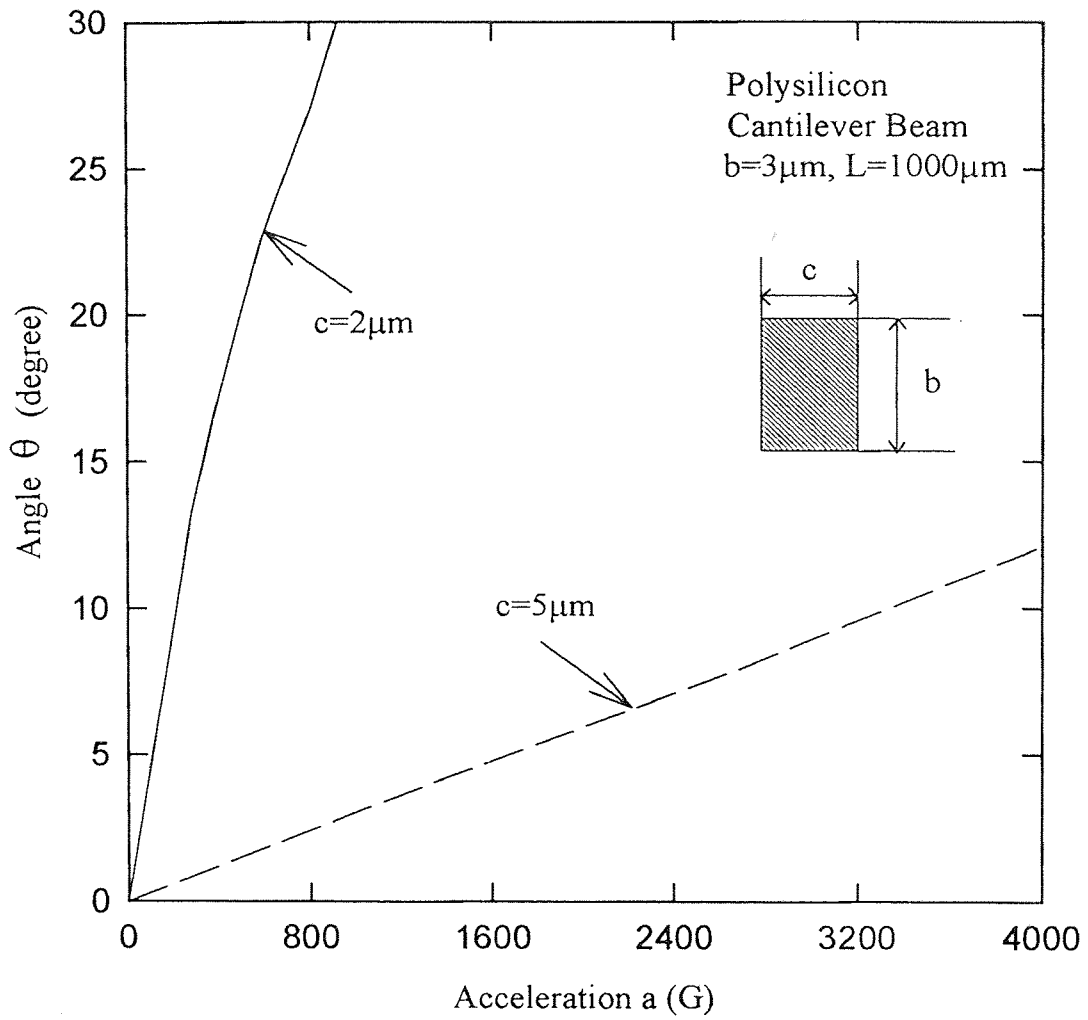
Figure 2.8 The relation of acceleration and deflection angle neglecting friction (L=1000μm)

2.4 Coordination of Deflected Tip Neglecting Friction

Now we will determine the dimension of the friction tether for the accelerometer.

The exact expression for the curvature of the elastic line may be stated conveniently in terms of arc length and slope angle denoted by s and θ, respectively. If x is the horizontal coordinate measured from the fixed end of the beam, the product of EI and the curvature of the beam equals the bending moment M:

$$EI\frac{d\theta}{ds}=P(L\text{-}x)=M \tag{2.16}$$

or

$$\frac{d^2\theta}{ds^2} = -\frac{P}{EI}\frac{dx}{ds} = -\frac{P}{EI}\cos\theta \tag{2.17}$$

Whence

$$\frac{1}{2}(\frac{d\theta}{ds})^2 = -\frac{P}{EI}\sin\theta + C \tag{2.18}$$

The constant C can be evaluated directly by observing that the curvature at the loaded end is zero. If θ_0 is the corresponding angle of slope

$$\frac{d\theta}{ds} = \sqrt{\frac{2P}{EI}}(\sin\theta_0 - \sin\theta)^{\frac{1}{2}} \tag{2.19}$$

The value of θ_0 cannot be found directly from this equation but it is implied by the requirement that the beam be inextensible, so that

$$\sqrt{\frac{2P}{EI}} \int_0^L ds = \int_0^{\theta_0} (\sin\theta_0 - \sin\theta)^{-\frac{1}{2}} d\theta = \sqrt{2}(\frac{PL^2}{EI})^{1/2} \qquad (2.20)$$

In order to evaluate this elliptic integral, denote PL^2/EI by α^2 and let

$$1 + \sin\theta = 2k^2 \sin^2\phi = (1 + \sin\theta) \sin^2\phi \qquad (2.21)$$

Then we have a classic elliptical integral of the first kind

$$\alpha = \int_{\phi_1}^{\pi/2} (1 - k^2 \sin^2\phi)^{-1/2} d\phi, \qquad (2.22)$$

Where $\sin\phi_1 = \dfrac{\sqrt{2}K}{2}$.

The next step is to represent the deflection δ in terms of α and an elliptic integral. since

$$\frac{dy}{d\theta}\frac{d\theta}{ds} = \frac{dy}{ds} = \sin\theta, \qquad (2.23)$$

and since we have $d\phi/ds$ from Equation 2.19 get

$$\frac{dy}{d\theta}\sqrt{\frac{2P}{EI}}(\sin\theta_0 - \sin\theta)^{1/2} = \sin\theta \qquad (2.24)$$

thus

$$\delta_y = \int_0^y dy = \sqrt{\frac{EI}{2P}} \int_0^\theta \frac{\sin\theta d\theta}{(\sin\theta_0 - \sin\theta)^{1/2}} \qquad (2.25)$$

with the aid of Equation (2.21) we obtain

$$\frac{\delta_y}{L} = \frac{\sqrt{2}}{2\alpha} \int_0^{\theta_0} \frac{\sin\theta d\theta}{(\sin\theta_0 - \sin\theta)^{1/2}} = \frac{1}{\alpha} \int_{\phi_1}^{\pi/2} \frac{(2k^2 \sin^2\phi - 1)d\phi}{(1 - k^2 \sin^2\phi)^{1/2}} \qquad (2.26)$$

This equation can be split up into complete and incomplete elliptic integrals of the first and second kinds.

$$\frac{\delta_y}{L} = \frac{1}{\alpha}[F(k) - F(k,\phi_1) - 2E(k) + 2E(k,\phi_1)] \qquad (2.27)$$

$$\alpha = F(k) - F(k,\phi_1) \qquad (2.28)$$

so that

$$\frac{\delta_y}{L} = 1 - \frac{2}{\alpha}[E(k) - E(k,\phi_1)] \qquad (2.29)$$

The vertical deflection at the end of the cantilever beam is

$$\frac{\delta_y}{L} = 1 - \sqrt{\frac{4EI}{PL^2}}(E(k) - E(k,\phi)) \qquad (2.30)$$

in which

E(k) = complete elliptic integral of the second kind

$$= \int_0^{\frac{\pi}{2}} \sqrt{1 - k^2 \sin^2 t}\, dt \qquad (2.31)$$

E(k,ϕ) = elliptic integral of the second kind

$$= \int_0^{\phi} \sqrt{1 - k^2 \sin^2 t}\, dt \qquad (2.32)$$

The horizontal deflection δx of the load cantilever beam is

$$P(L - \delta_x) = EI\left(\frac{d\theta}{ds}\right) = EI\sqrt{\frac{2P}{EI}}(\sin\theta_0)^{1/2} \qquad (2.33)$$

or

$$\frac{L - \delta_x}{L} = \frac{\sqrt{2}}{\alpha}(\sin\theta_0)^{1/2} \qquad (2.34)$$

so

$$\frac{\delta_x}{L} = 1 - \sqrt{\frac{2EI\sin\theta}{PL^2}} \qquad (2.35)$$

we get the relation of δ_x, δ_y and θ in figure 2.9-2.11.

Figure 2.9 Coordination (δx, δy) of the deflected tip of the cantilever beam as a function of acceleration a for the case of no friction and at maximum deflection (L=250μm)

Figure 2.10 Coordination (δx, δy) of the deflected tip of the cantilever beam as a function of acceleration a for the case of no friction and at maximum deflection (L=500μm)
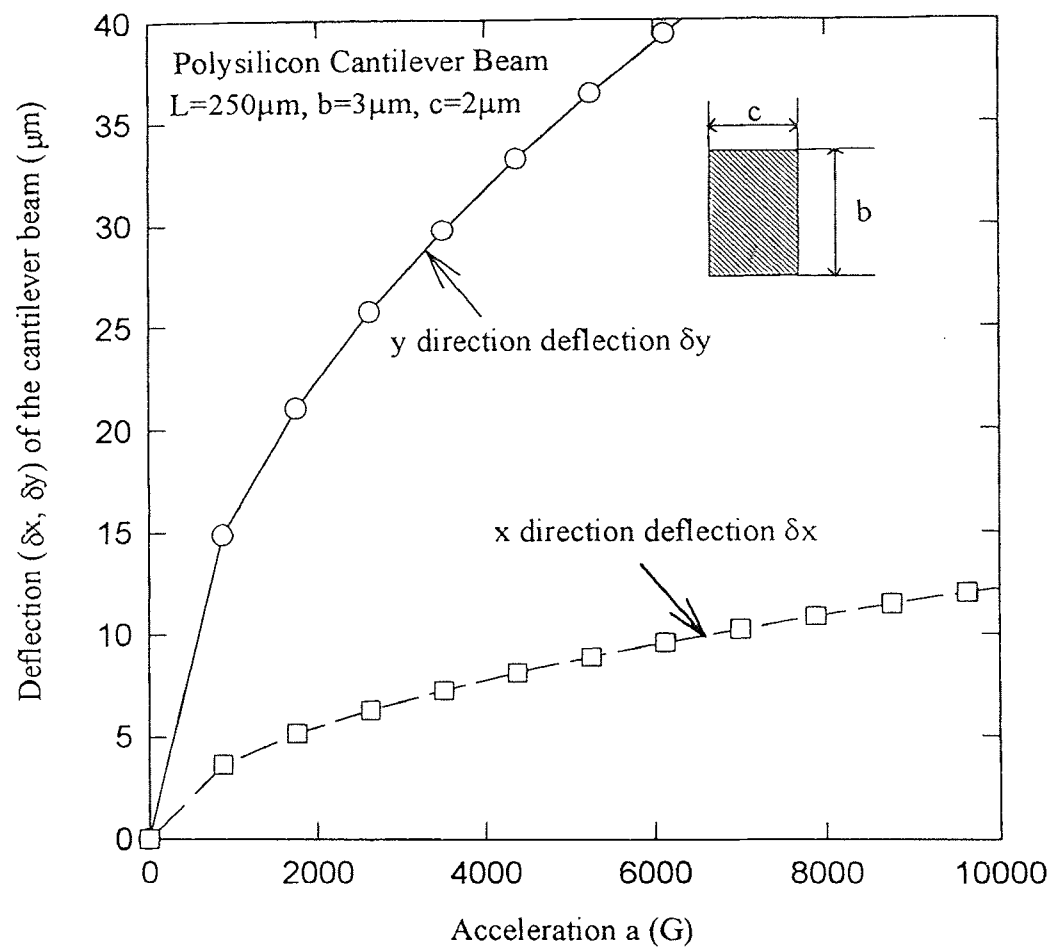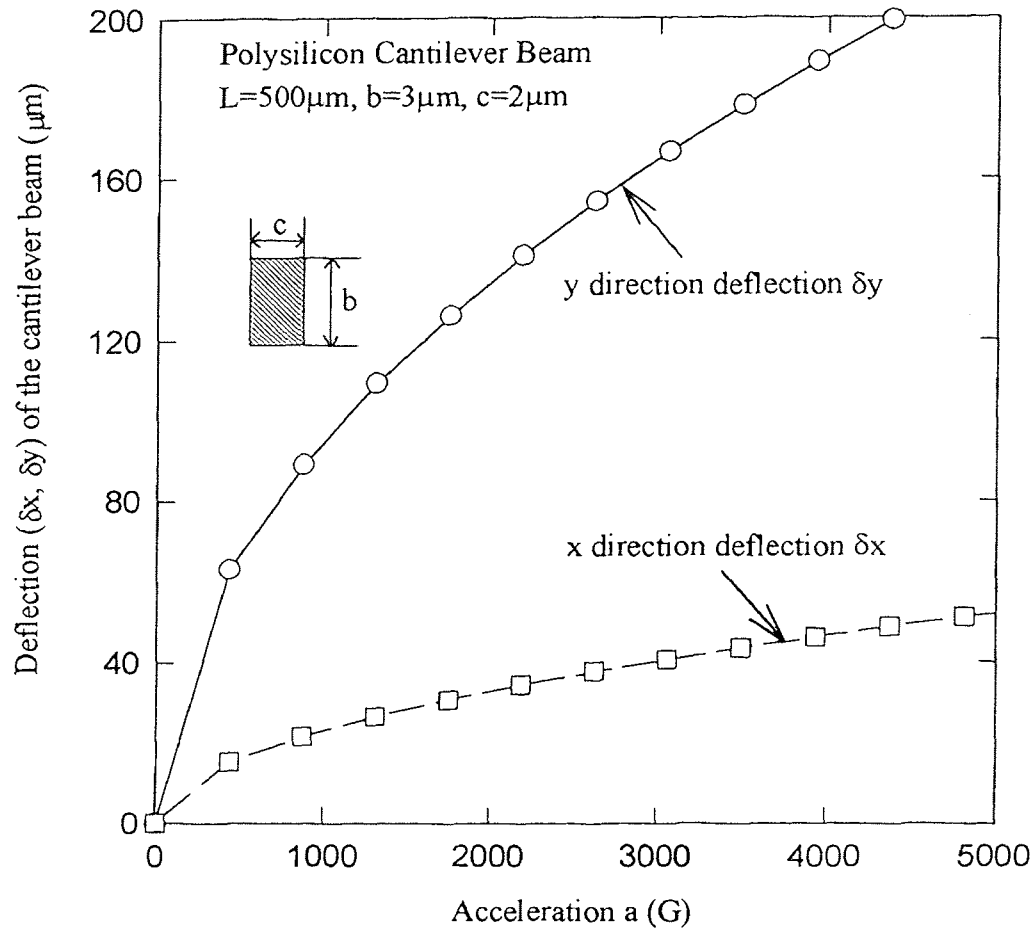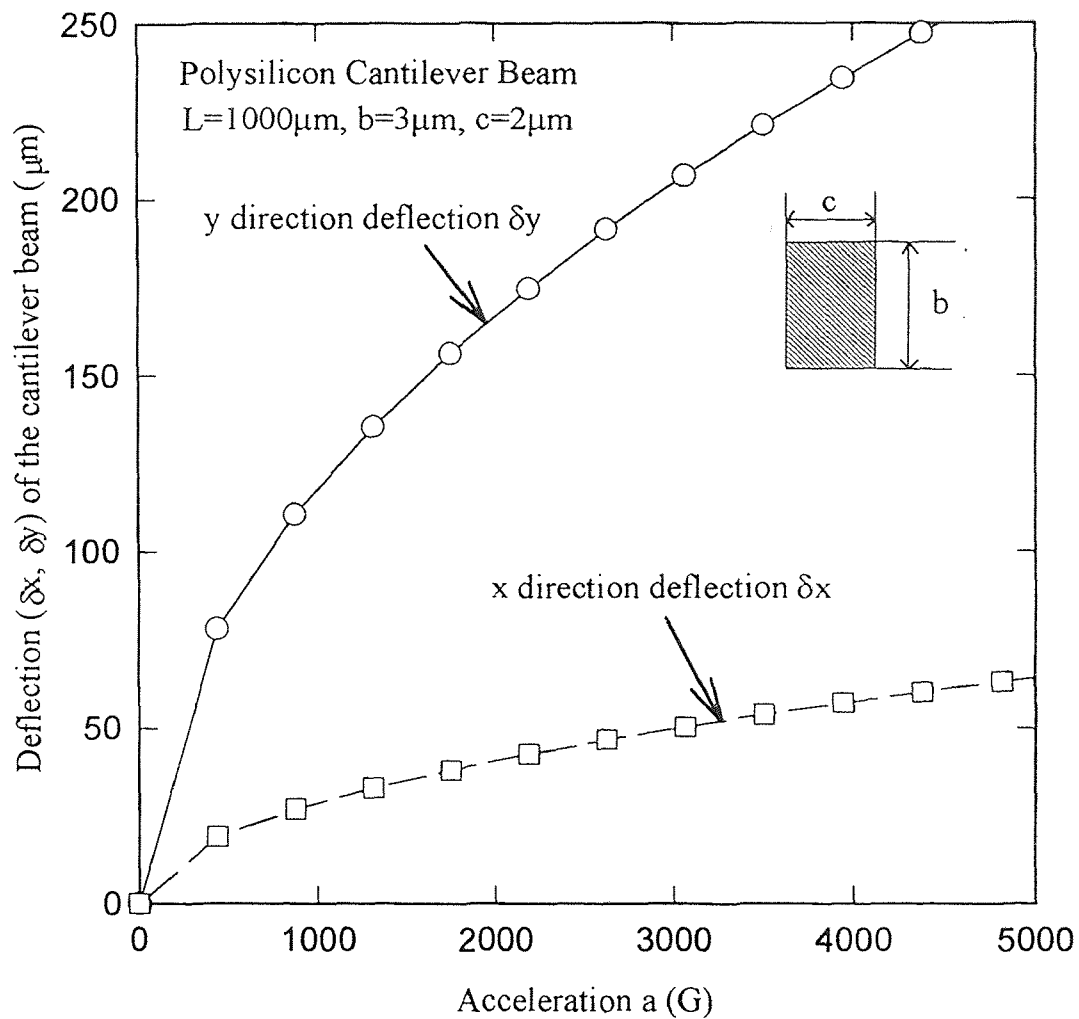
Figure 2.11 Coordination (δx, δy) of the deflected tip of the cantilever beam as a function of acceleration a for the case of no friction and at maximum deflection (L=1000μm)

CHAPTER 3

PHYSICAL DATABASE PHOTOMASK DESIGN

3.1 Polysilicon Layer Design

From the last chapter, the author has determined the dimension of the cantilever beam, the etching hole, so eight cantilever beam will be designed, to save the space and minimize the dimension of the whole device, we used one support pedestal at the center, and eight cantilever beams around it, like a radiator. The top view of the combined three layers and the polysilicon layer is in Figure 3.1,3.2.

The eight design is:

1. Length L= 500μm, Width c=5μm, thick b=3μm

2. L= 1000μm, c=5μm, b=3μm

3. L=500μm, c=10μm, b=3μm

4. L=1000μm, c=2μm, b=3μm

5. L=500μm, c=2μm, b=3μm

6. L=250μm, c=10μm, b=3μm

7. L=250μm, c=2μm, b=3μm

8. L=250μm, c=5μm, b=3μm

To see more clearly, we separate the whole device into parts.

The support pedestal is in the center of Figure 3.2, because the author uses Mentor Graphics to draw the cantilever beam and support pedestal separately, and it is easy for revise and on the other hand is that they must be fabricated as a whole part, so I choose the cantilever beam is 2μm into the support pedestal, the length of each edge is 80μm.
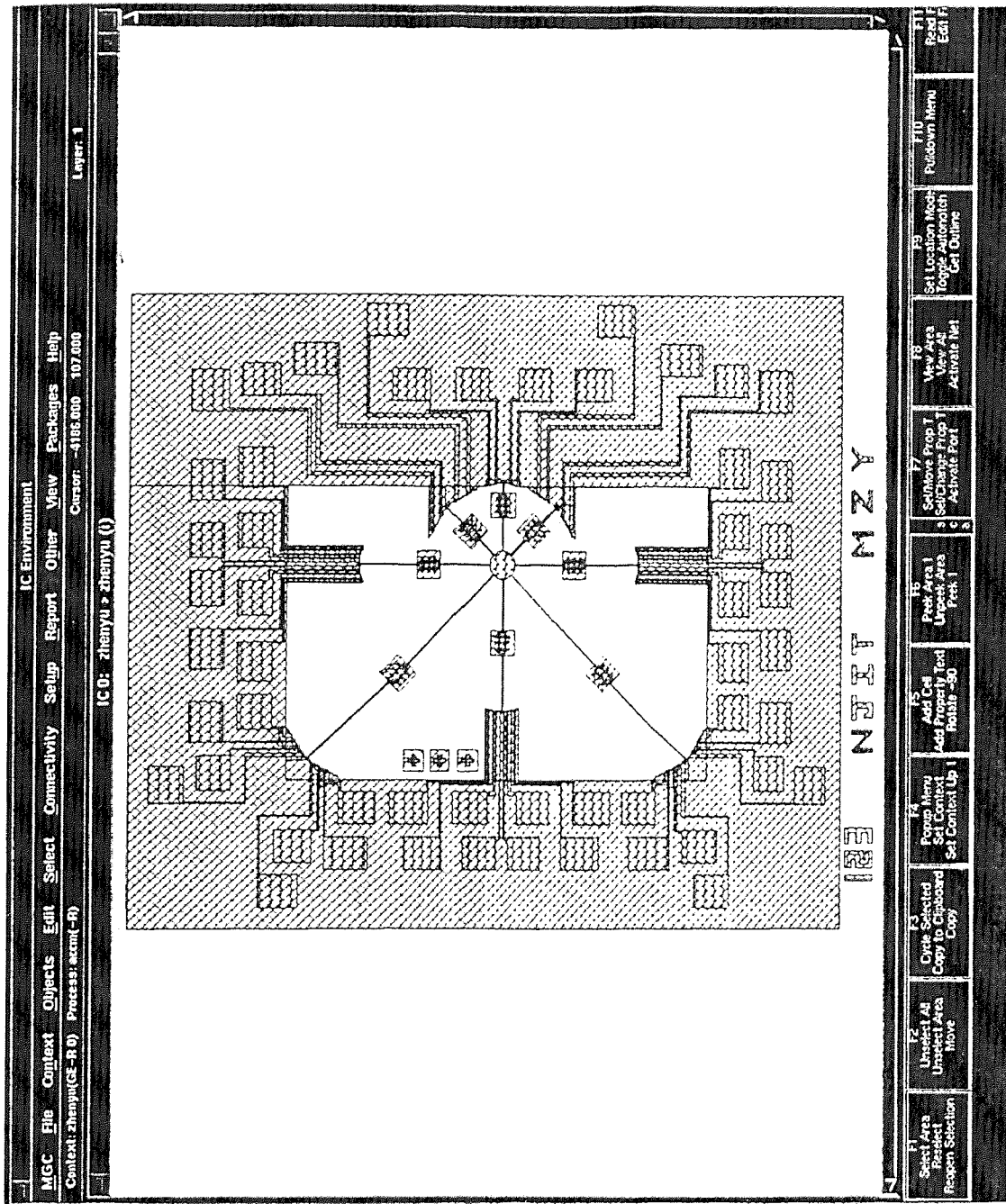
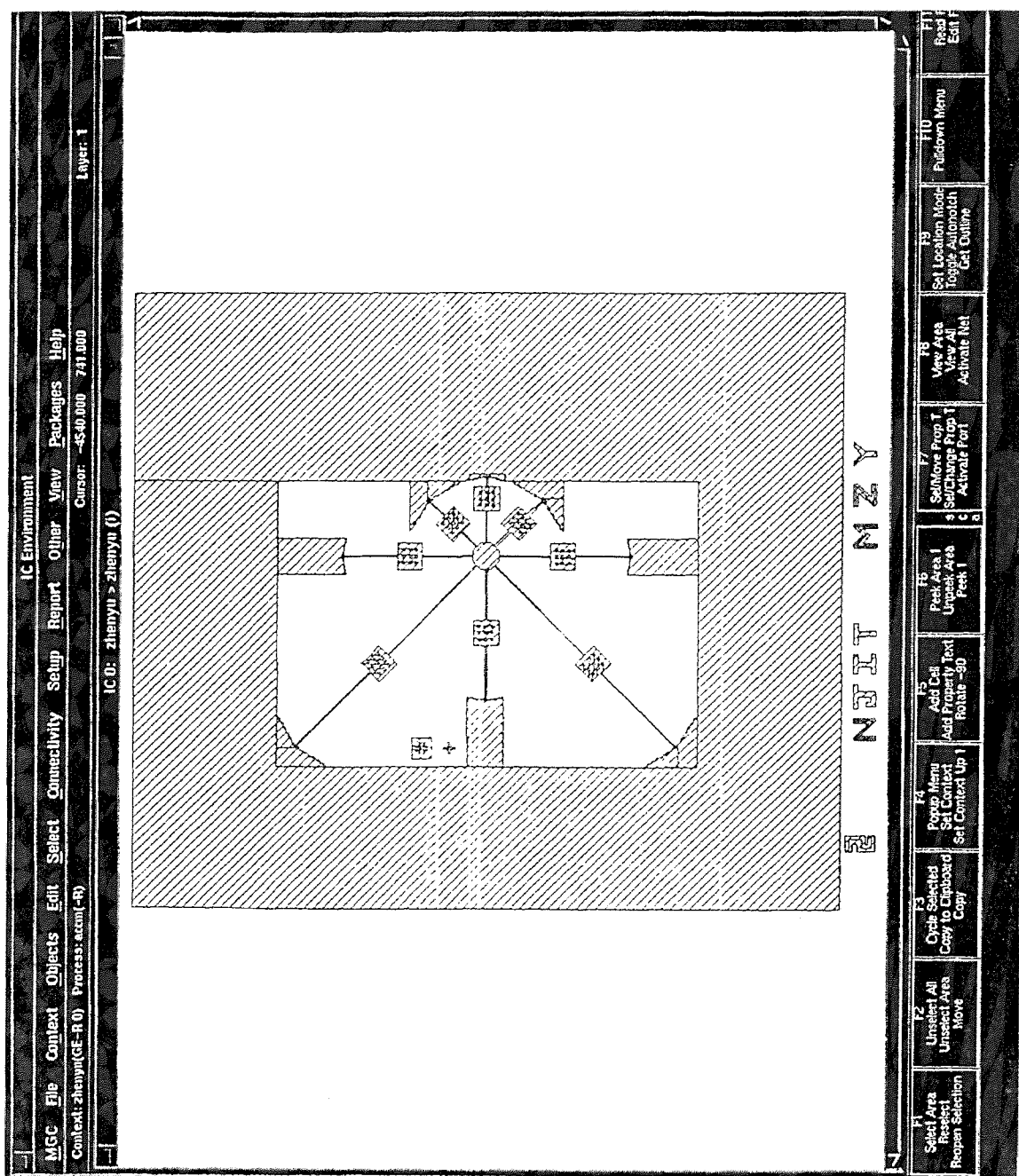**Figure 3.1** Top view of the three-layer masks

Figure 3.2 Top view of the polysilicon layer mask

3.2 Etch Hole

Silicon dioxide(SiO_2) is used in micromachining as an amorphous film. The film etches isotropically because of this randomness. Therefore, underetching is possible.

We use the HF in the etching, for the mass of the cantilever beam is 100μ m*100μm, etching the under oxide needs a long time, some etching hole have been opened on the mass to improve etching condition, shorten the etch time, and also it can get a good etch effect.

The dimension of the etching hole is 10μm*10μm square, the largest distance between two etching holes is 20μm. So on the mass we open 9 etch holes. It will cut the etch time to 1/5 of the original. For the balance of the mass, the etching hole must be symmetric, the design can be seen in figure 3.2.

3.3 Oxidation Layer

The oxidation layer is a sacrificial layer for etching, the pattern is light, it is just reverse of the polysilicon layer (figure 3.2), but without the cantilever beam. The center of the oxidation layer is needed to be etched away for the support pedestal of the cantilever beam. It is an octagon design, eight different dimension cantilever beams are supported by it.

3.4 Aluminum Layer

For test, we add one layer of aluminum on top of polysilicon. The test principle is when an acceleration is added on the test device, the aluminum on the cantilever beam will contact on the aluminum of the friction tether, on each step to make a short circuit for test. It is shown on figure 3.3. Other metals such as Pt, Pd, Au can be used instead of aluminum for not oxide.
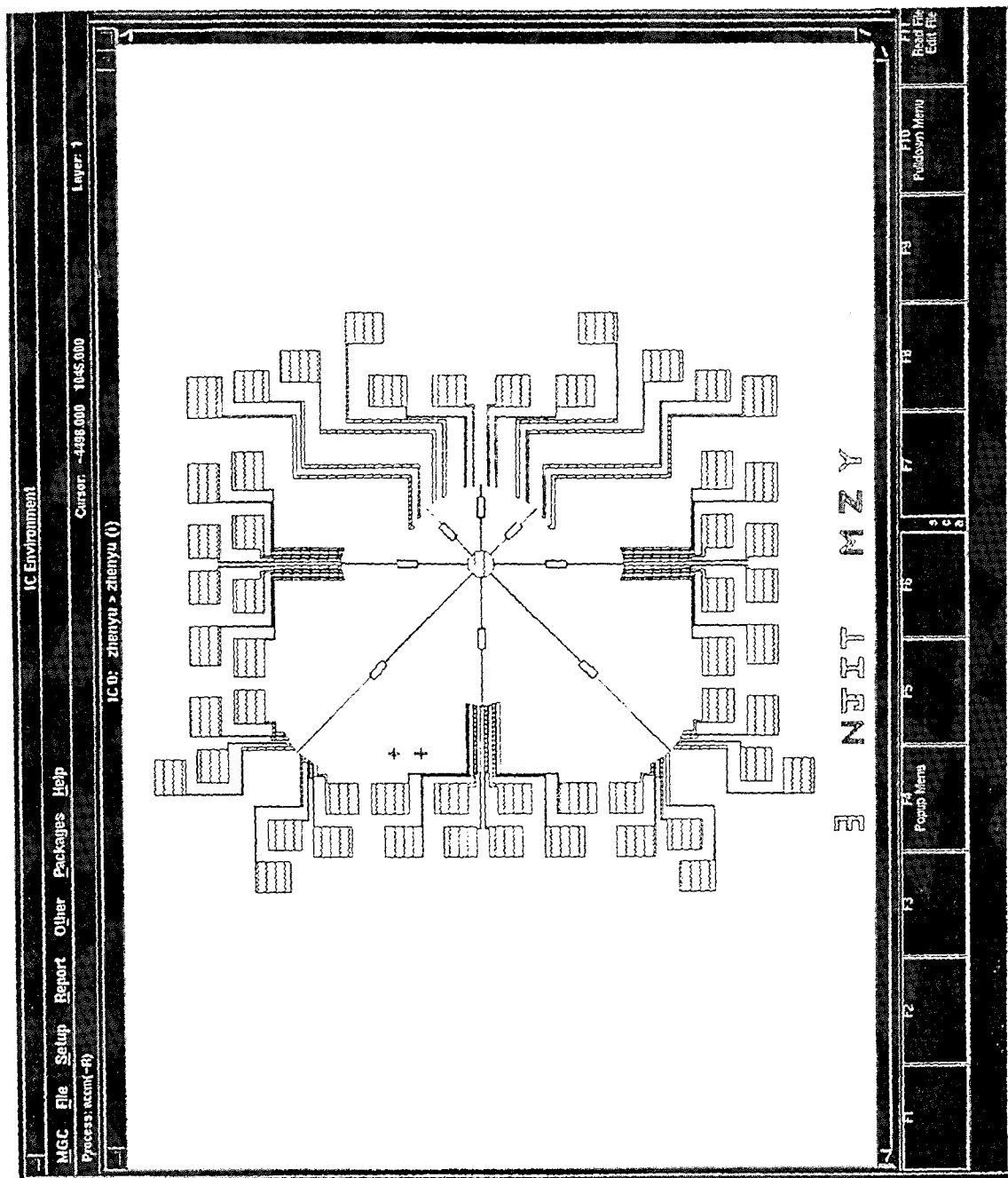
**Figure 3.3** Top view of the aluminum layer

CHAPTER 4

CLEANROOM PROCESSING DESIGN

4.1 LTO Deposition

There are various reactions that can be used to prepare CVD SiO_2. A deposition of LPCVD oxide (Low Temperature Oxidation) is used to create a stress-free silicon oxide. The deposition parameters that are important for CVD SiO_2 include: temperature, pressure, reactant concentrations and their ratios. Presence of dopant gases, system configuration, total gas flow, and wafer spacing. There are three temperature ranges in which SiO_2 is formed by CVD, each with its own chemical reactions and reactor configurations. These are: 1) low temperature deposition (300-450°c), 2) medium temperature deposition (650-750°c) and 3) high temperature deposition (~900°c).

The low temperature deposition of SiO_2 utilizes a reaction of silane and oxygen to form undoped SiO_2 films. The depositions are carried out in distributed feed LPCVD reactors. The depletion effect precludes the use of conventional LPCVD for the SiH_4+O_2 reaction.

$$SiH_4 + O_2 \rightarrow SiO_2 + 2H_2$$
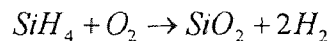
The deposit rate increase slowly with increased temperature between 310°c and 450°. The deposition rate can be increased at constant temperature (up to a limit) by increase the O_2: SiH_4 ratio.

Silicon dioxide films deposited at low temperatures exhibit lower densities than thermal SiO_2, they also exhibit substantially higher etch rates in buffered hydrofluoric

acid (HF) solutions than thermal SiO_2. So it is used as a sacrificial layer for micro sensor.

4.2 Polysilicon Deposition

Thin layer of polysilicon are usually formed by chemical vapor deposition (CVD) using the pyrolysis (thermal decomposition) of silane (SiH_4) to form solid silicon. For thicker layers, chlorinated compounds, such as dichlorosilane (SiH_2Cl_2) or silicon tetrachloride (SiH_4) are often used to obtain high deposition rate. To fabricate sensors, polysilicon is usually deposited on a dielectric layer, quite often silicon oxide.

As with the transition between amorphous and polycrystalline silicon, the preferred orientation or 'texture' of continuous film is greatly influenced by surface migration of the adsorbed silicon atoms during deposition.

Figure 4.1 shows the preferred orientation as a function of deposition temperature in polysilicon films deposited at low pressures (a fraction of a Torr)
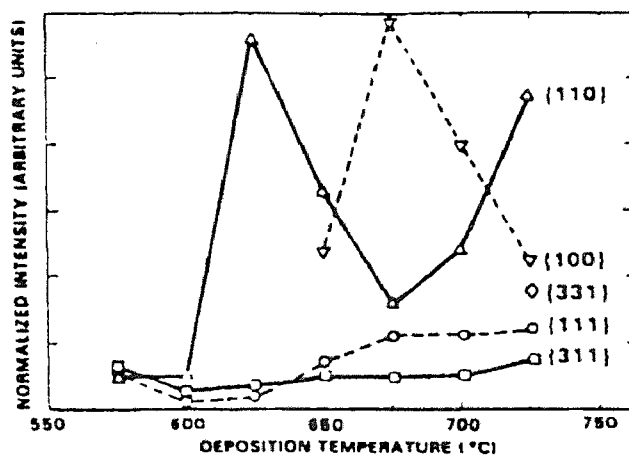
Figure 4.1 Preferred orientations in polycrystalline silicon films deposited at low pressures (≈ 0.1 -1 Torr) [26].

The thick films is deposited at which considerable rearrangement of the silicon atoms can occur after they are covered by subsequently arriving atoms.

The resulting volume contraction can lead to the tensile stress usually found in these films [26][27].

Films deposited at lower temperatures in an amorphous form are unstable and crystallize readily during annealing at only moderate temperatures.

In figure 4.2, films deposited in an amorphous form at 580°c are crystalline after annealing at 800°c, and can crystallize during long heat treatments at temperatures as low as about 600°c.
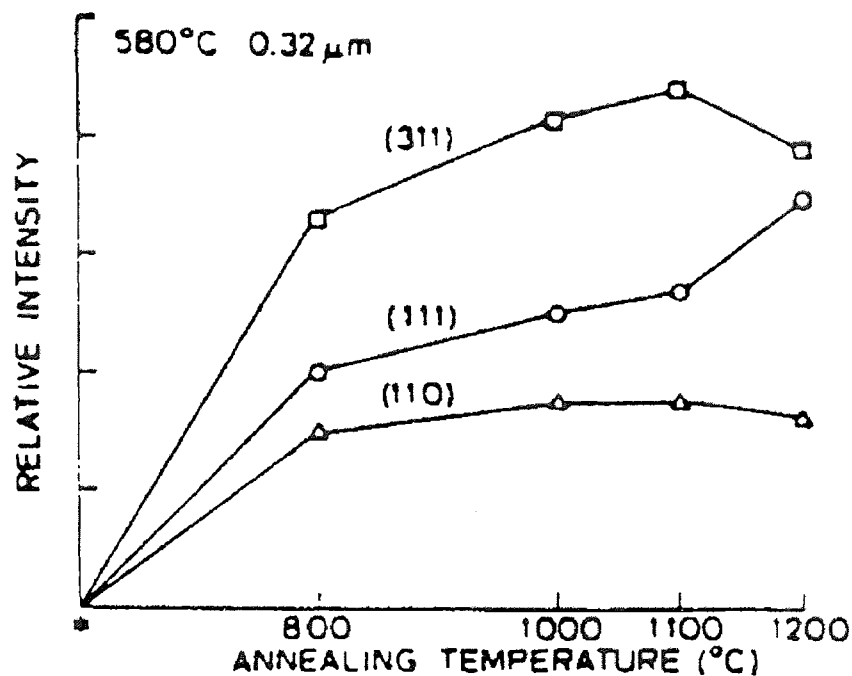

Figure 4.2 Effect of annealing on dominant grain orientations in silicon films deposited in an LPCVD reactor in an initially amorphous form at 580°C. [27]

4.3. RIE of Polysilicon

Polysilicon etching is performed by using the fluorine containing gases such as CF_4, SF_6 and NF_3. At high pressures, etching is more or less isotropic, and a very high selectivity over SiO_2 (up to 100:1) can be obtained. At low pressures (1-3 Pa) anisotropic etching is possible because of enhanced ion bombardment.

The concepts of RIE system is followed the reactive ion etching system is shown in Figure 4.3 with voltage potential distributions between the anode and the cathode. The figure shows the block diagram of typical reactive ion etch. This system has an asymmetrical electrode structure. Between electrode and plasma, a Crooke's dark space is formed.
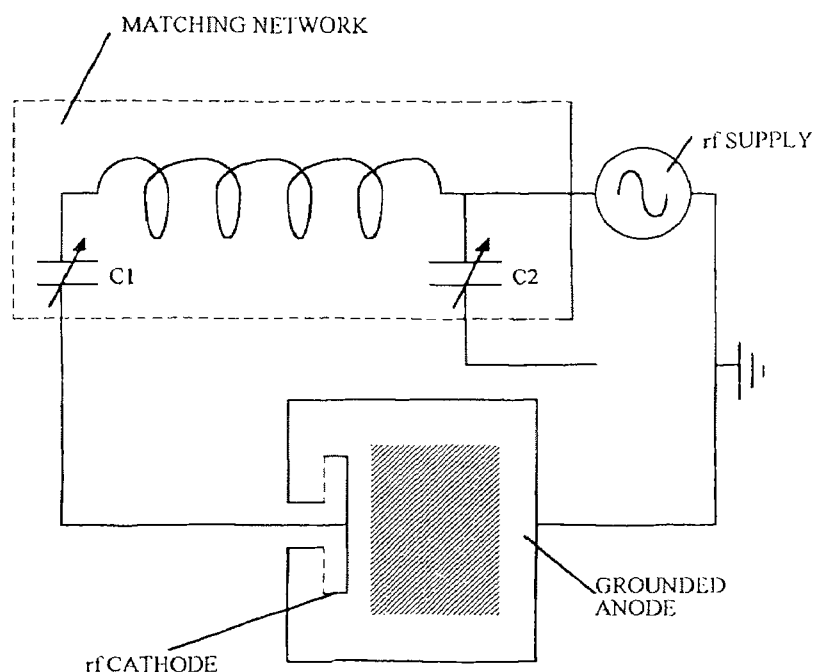

Figure 4.3 Schematic representation of reactive ion etching system

Positive ions are created and accelerated primarily in the dark space. The potential difference across the dark area is an important parameter for the ion etching and is given by

$$v_p - v_{fi} = \frac{KTe}{2e} \ln \frac{MiTi}{MeTe}$$ (4.1)

where v_p, Me, Mi, v_{fi}, Te and Ti are plasma potential, mass of electron and ion, substrate potential and temperature of electrons and ions respectively.

Since the plasma has a very low electric field, the space within the plasma is essentially equipotential at v_p. If an isolated substrate is inserted into the plasma, the substrate takes on a "floating potential" v_{fi}. The plasma potential v_p is always greater than the floating potential v_{fi}. This potential v_p-v_{fi} drives ions up against the substrate and enhances ion etching process.

Figure shows the potential distributions with v_a and v_c which are the anode and the cathode potentials, respectively. The substrate is mounted on the cathode with v_c. The potential difference between the cathode and plasma plays a major role of the acceleration of the ions and the electrons in the system.

In order to provide maximum of power delivery in the system, the capacitance for impedance matching should be adjusted in Figure.

4.4 Wet Etching of Silicon Dioxide

Wet etching of SiO_2 films in microelectronic applications is usually accomplished with various hydrofluoric acid (HF) solutions. This is because SiO_2 is readily attacked by room temperature HF, while Si is not, etching takes place according to the overall equation

$$SiO_2 + 6HF \rightarrow H_2 + SiF_6 + 2H_2O$$
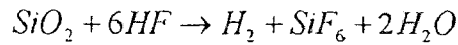
The concentration of HF supplied by chemical manufactures is 49% in water, such concentrated HF, however, etches SiO_2 too quickly for good process control. Thus diluted HF is generally used instead. A common etchant formulation contains buffering agents such as ammonium fluoride (NH_4F) which help prevent depletion of the fluoride ions, and thus maintain stable etching characteristics.

The etch rate of SiO_2 for a given etchant and temperature also depends on several other factors. For example the presence of impurities in the oxide strongly affect the etch rate. A high concentration of boron results in a reduced etch rate, while a high concentration of phosphorus rapidly increases it.

CVD SiO_2 generally etches much more rapidly than thermally grown SiO_2, but this rate depends on many other factors, including deposition conditions, impurity concentration, and densifying heat treatments after deposition. As a general rule, SiO_2 films deposited at low temperatures exhibit higher etch rates than films annealed or deposited at higher temperatures, CVD SiO_2 is more commonly etched in diluted HF etches, since slower and more controllable etch rates can be achieved.

4.5 Processing of Mechanically-latched Accelerometer

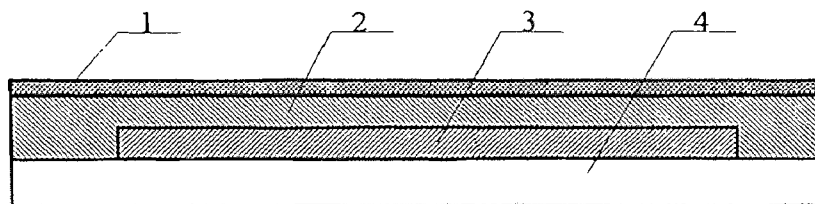The cross section of this design is in figure 4.4, processing steps are as follows:

Figure 4.4 Cross section of the mechanically-latching accelerometer
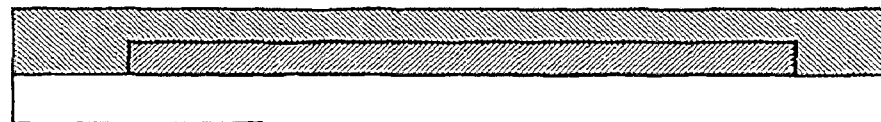1. Aluminum 2. Polysilicon 3. Silicon Dioxide 4. Silicon Substrate

Step 1 Wafer clean
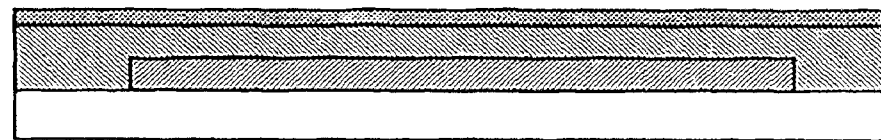
Step 2 Silicon dioxide growth by LTO (1μm)
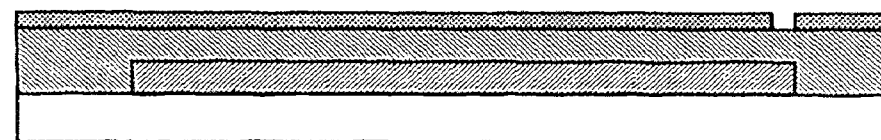
Step 3 Open oxide for support pedestal and friction tether (mask 1)
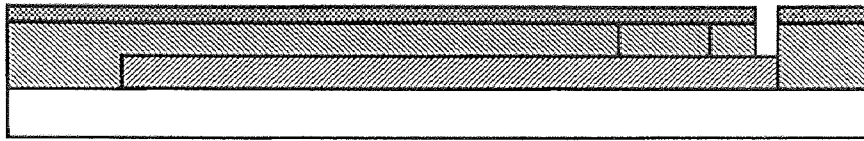Step 4 Oxide etch by BOE (1μm depth)

Step 5 Polysilicon deposition by LPCVD (2μm)

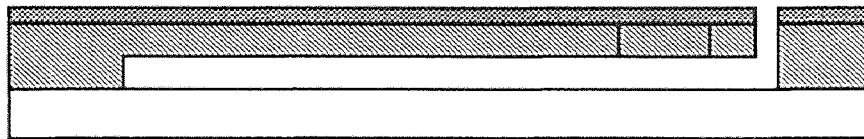Step 6 Aluminum deposition by sputtering (3000Å)

Step 7 Aluminum etch (mask 2)

Step 8 Polysilicon cantilever beam definition (mask 3)
Step 9 Polysilicon etch

Step 10 Sacrificial layer SiO_2 be removed by HF etch

CHAPTER 5

DEVICE TEST

5.1 Test Goal

To generate the acceleration added on the structure, we want to set up a test circuit to output a sinusoidal wave. The equation for this device is

$$X = A_0 \sin(\omega t) \tag{5.1}$$

where ω is the sinusoidal wave frequency and

A_0 is the amplitude

Therefore
$$\ddot{X} = -A_0 \omega^2 \sin(\omega t) \tag{5.2}$$

Thus the Acceleration amplitude is
$$a = \frac{\sqrt{2}}{2} A_0 \omega^2 \tag{5.3}$$

The relation between a and ω is shown in Figure 5.1. An audio-frequency linear power amplifier is used to generate the acceleration at the center point of the loudspeaker. Several major problems associated with amplifiers must be considered and solved. The aim is to furnish the required power as economically as possible while meeting other specifications which may include limitations on size, weight, dc supply voltage, distortion, etc. Often the transistors are driven to the limits of their useful operating range, and careful design is required to ensure that physical damage due to excessive heating or otherwise does not occur.
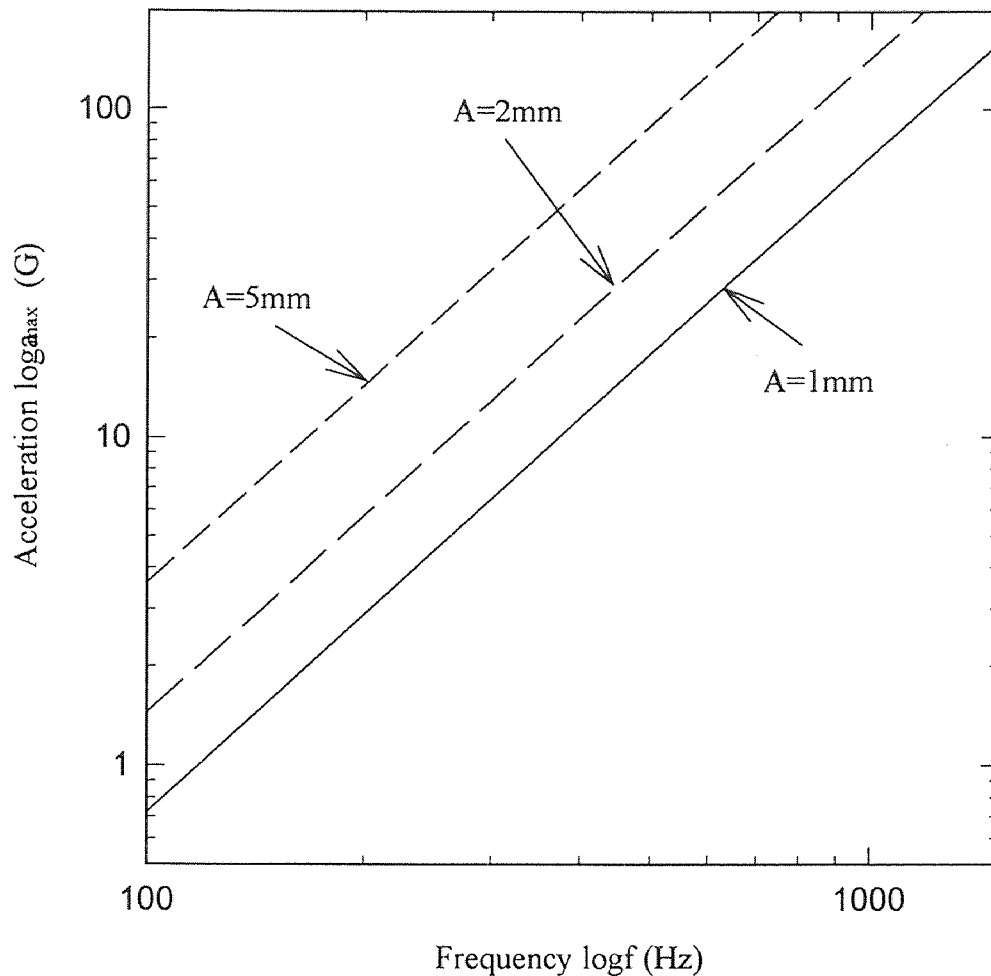
Figure 5.1 Maximum acceleration a_{max} as a function of audio frequency

Power amplifiers are classified according to the portion of input sine-wave cycle during which load current flow. the maximum attainable efficiency in class A operation is 50% because the peak ac collector current never exceeds the quiescent collector current. In the class B amplifier, the dc collector current is less than the peak ac current, thus less collector dissipation results, and the efficiency increases. One type [28] of the class B push-pull amplifier is shown in figure 5.2. The input and output result is on figure 5.3. From figure 5.3, you can see on the first half--cycle, i_{b_1} is zero, and because T_1 is biased at
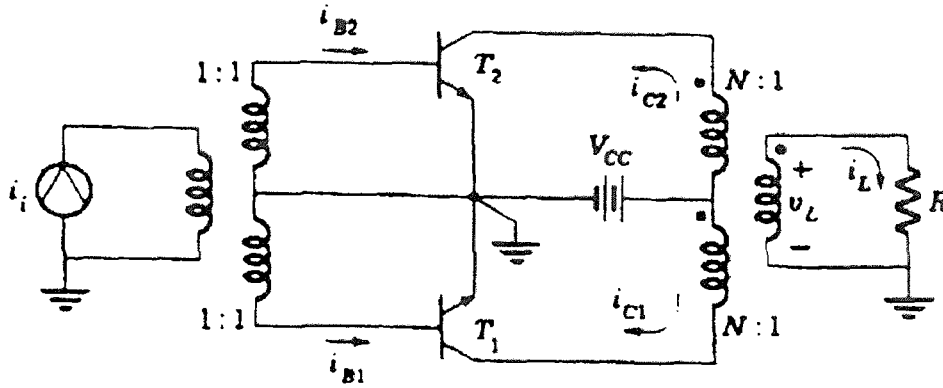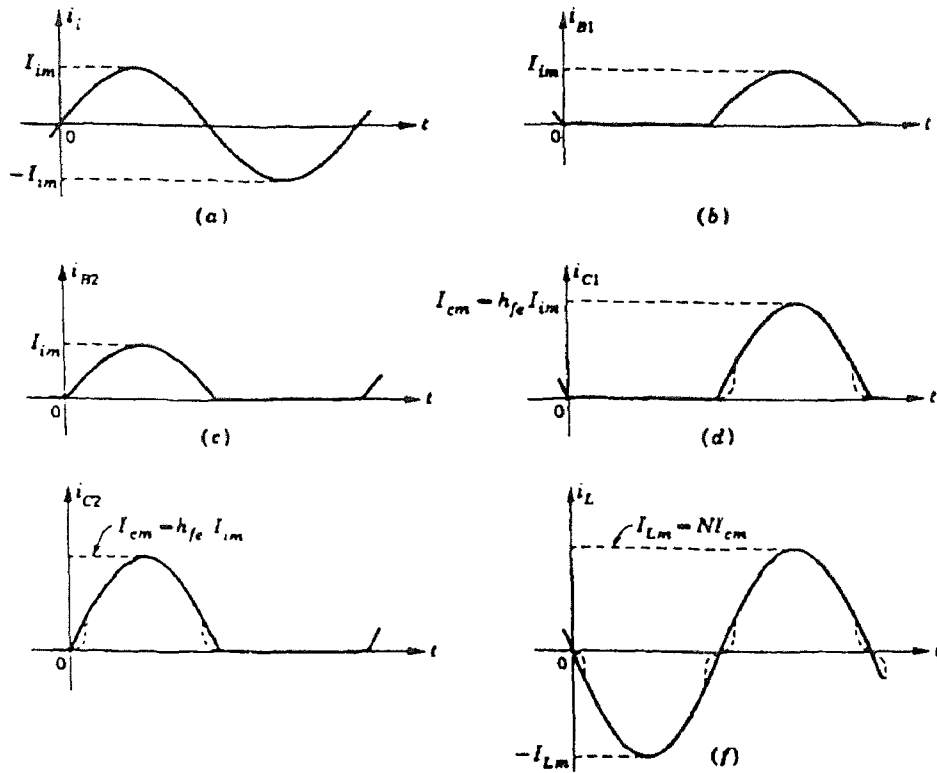
Figure 5.2 Push-pull amplifier

Figure 5.3 Wave forms in the push-pull amplifier. (a) input current; (b) base current in T_1; (c) base current in T_2; (d) collector current in T_1; (e) collector current in T_2; (f) load current

cutoff, i_{c_1} is zero as in (d) of the figure, however, in this same internal, i_{c_2} is positive, T_2 conducts, and the collector current i_{c_2} is shown in (e). Thus one transistor is cutoff, while the other is conducting. On the second half-cycle, the roles are reversed, T_2 is cutoff, and T_1 conducts. When T_2 conducts, the current shown in (e) flows through the upper half of the primary winding, and the resulting time-varying flux in the transformer core induces a voltage in the secondary winding. This voltage in turn, produces the first half-cycle of current through the load (f).

But this type of push-pull amplifier uses a lot of transformers, so the size and weight of this design is big. In this design, the principle of this design is used, and the structure is a complementary symmetrical push-pull amplifier.

5.2 Test Circuit

Figure 5.4 illustrates a type of class push-pull amplifier which employs one pnp and one npn transistor and requires no transformers. This type of amplifier uses complementary symmetry. Its operation can be explained by referring to the figure. When the signal current is positive, the npn transistor conducts while the pnp transistor is cut off. When the signal current is negative, pnp transistor conducts while npn transistor is cutoff. The load current is

$$i_L = i_{Q_1} - i_{Q_2} \tag{5.4}$$

The input and output current for this amplifier is showed in figure 5.5

Some advantage of the circuit are that the transformerless operation saves on weight and cost, and "balanced" push-pull input signals are not required. Also it is possible to obtain greater power output, the efficiency is higher, and there is negligible power loss at no signal. Disadvantages are the need for both positive and negative supply voltages, and

the problem of obtaining pairs of transistors that are matched closely enough to achieve low distortion.

To calculate the parameters for this current, the load is a loudspeaker, output power is P_L=15W, R_L=8Ω,

Therefore I_L=($P_L/R_L)^{1/2}$=$(15/8)^{1/2}$=1.4A

for the signal voltage required to operate this amplifier assuming R_1, R_2 is infinite, then because the circuit is basically an emitter follower, the maximum signal v_i = v_{im}sin (ωt) must have a peak value of v_{cc} (this is v_{im}=v_{cc}) in order to transfer the full 15W to the load.
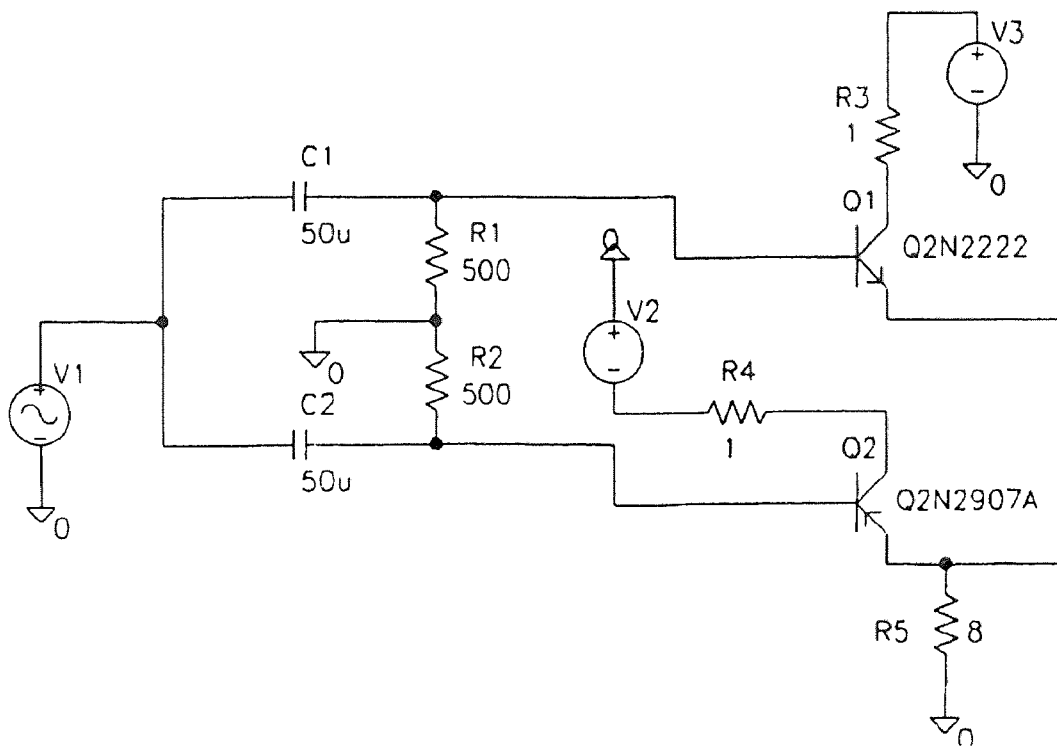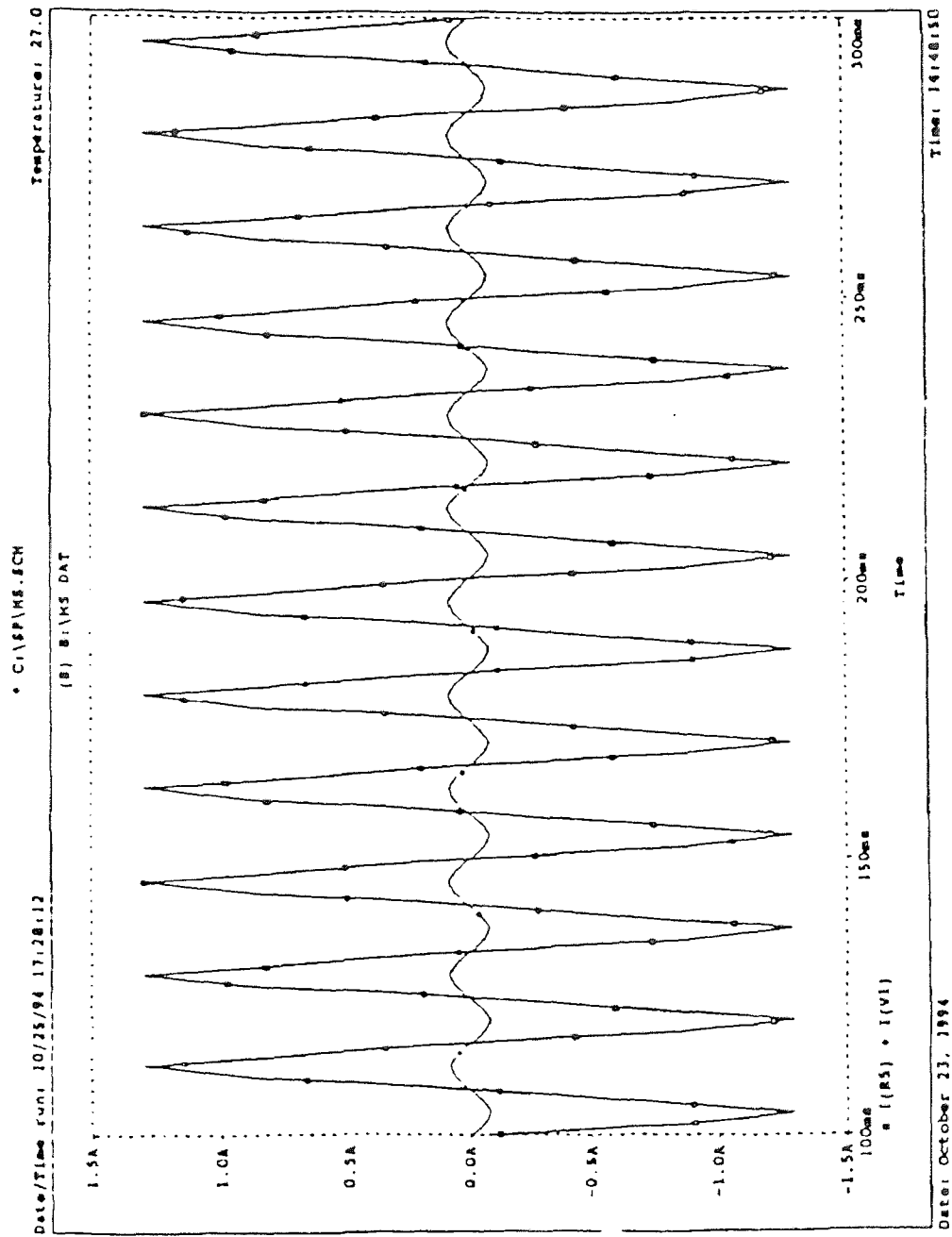
Figure 5.4 Test circuit

Figure 5.5 Input and output current of the test circuit

CHAPTER 6

CONCLUSION AND SUMMARY

This thesis contains the following six major summary points:

1. The designed acceleration sensitivity range is from 100G to 1000G.

2. The dimensions of the polysilicon cantilever beam have been calculated by using the large deflection of cantilever beam, the optimal width of the cantilever is between 2μm to 10μm, the optimal length of the cantilever beam is between 250μm to 1000μm, the optimal thickness of the cantilever is 3μm

3. The mechanically-latched arc around the cantilever beam is simulated and designed for read the acceleration out.

4. Three layers of mask have been drawn out on the Mentor Graphics system by using the dimensions designed in simulation.

5. The processing technique for fabrication of the microaccelerometer in the NJIT cleanroom is presented, and the process steps for fabrication in the NJIT cleanroom is discussed in detail and attached on the appendix.

6. The test circuit for generate the acceleration is designed and constructed, the input and output current related to the power for generating acceleration is simulated by using PSPICE software. By changing the frequency in the test circuit, the output acceleration can be controlled in the range from 0 to 200G.

This design thesis concludes that the latching microaccelerometer can be fabricated by using standard surface-micromaching techniques.

APPENDIX A

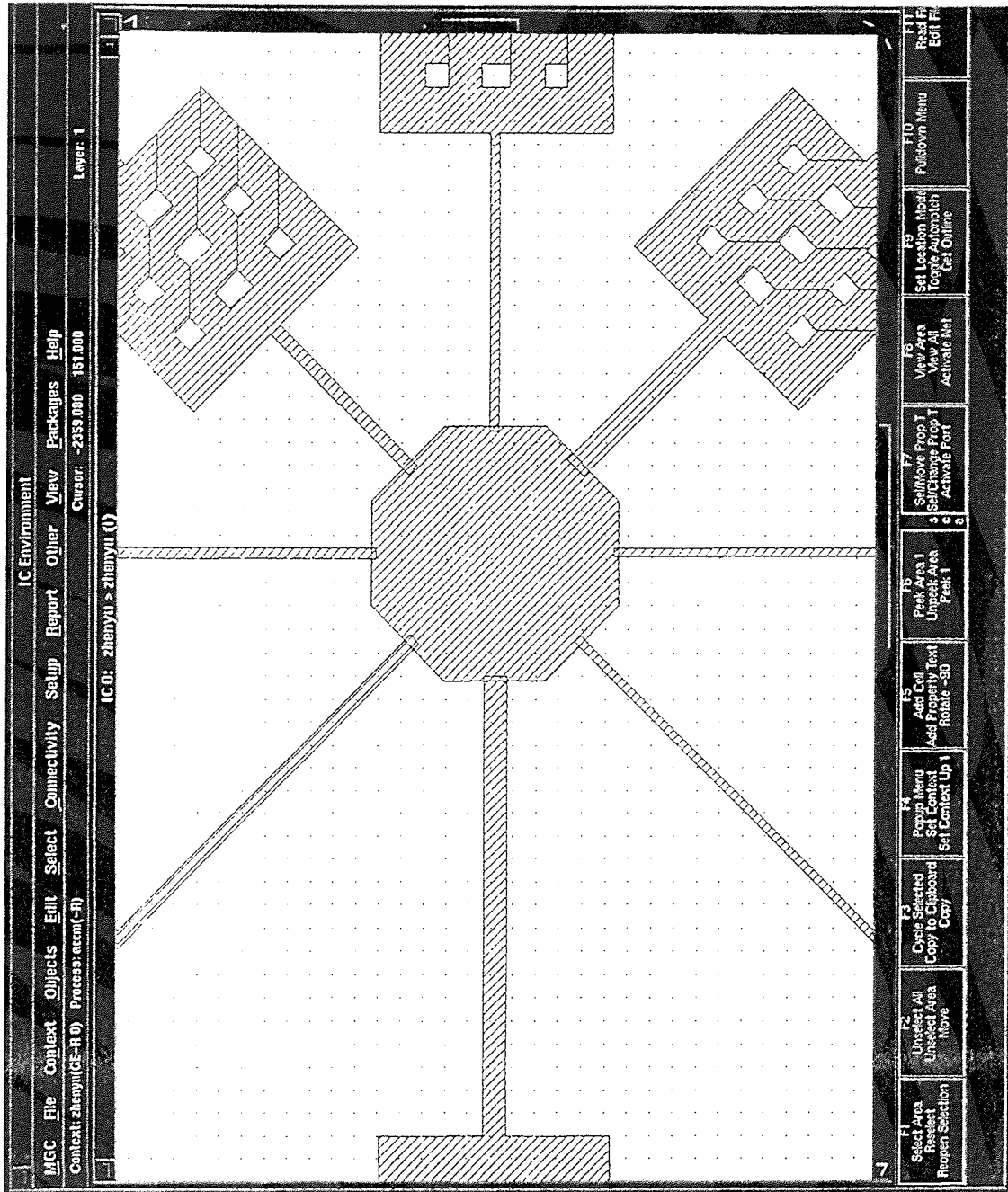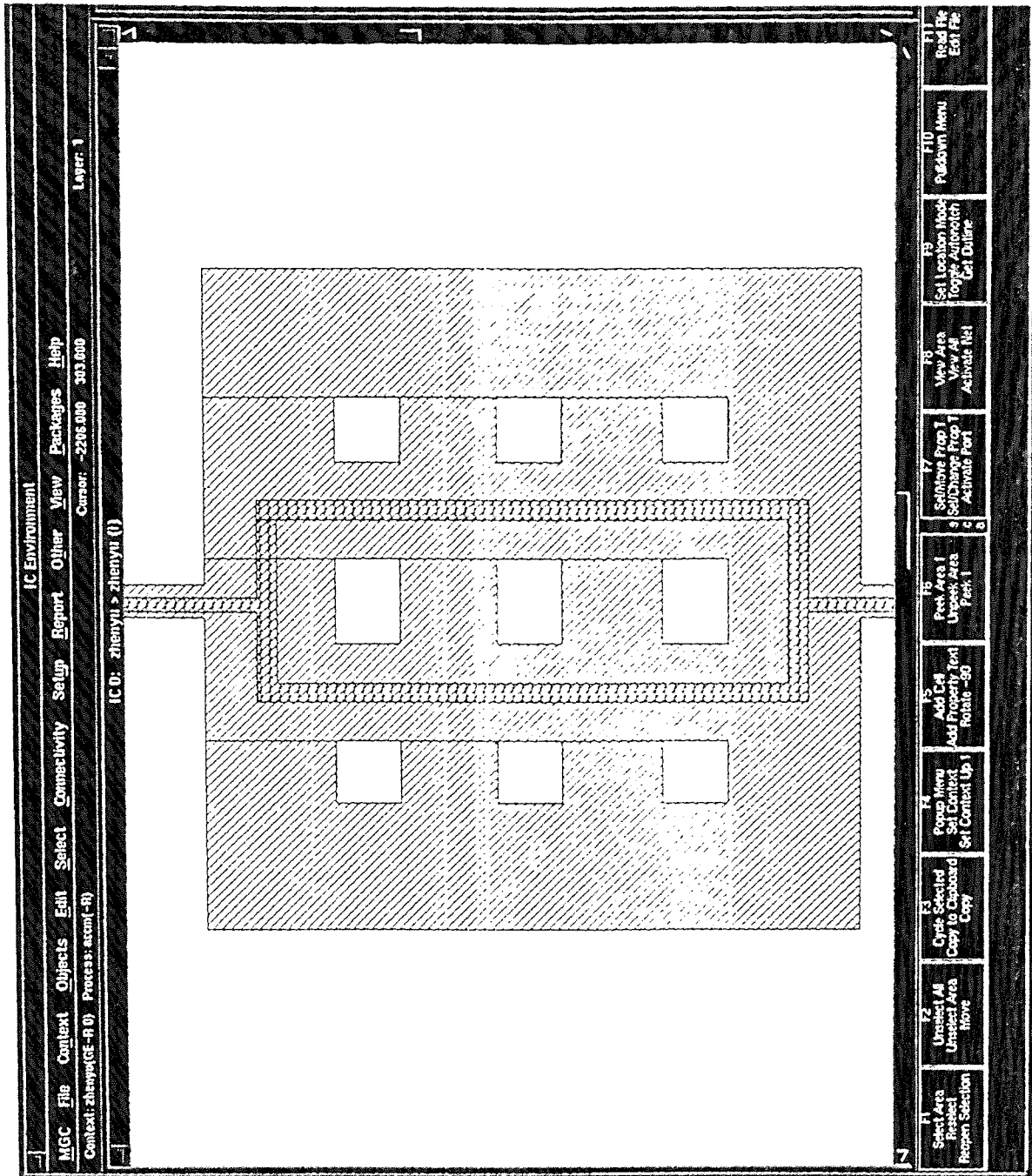# MASK LAYOUT

Figure A.1 Top view of the support pedestal
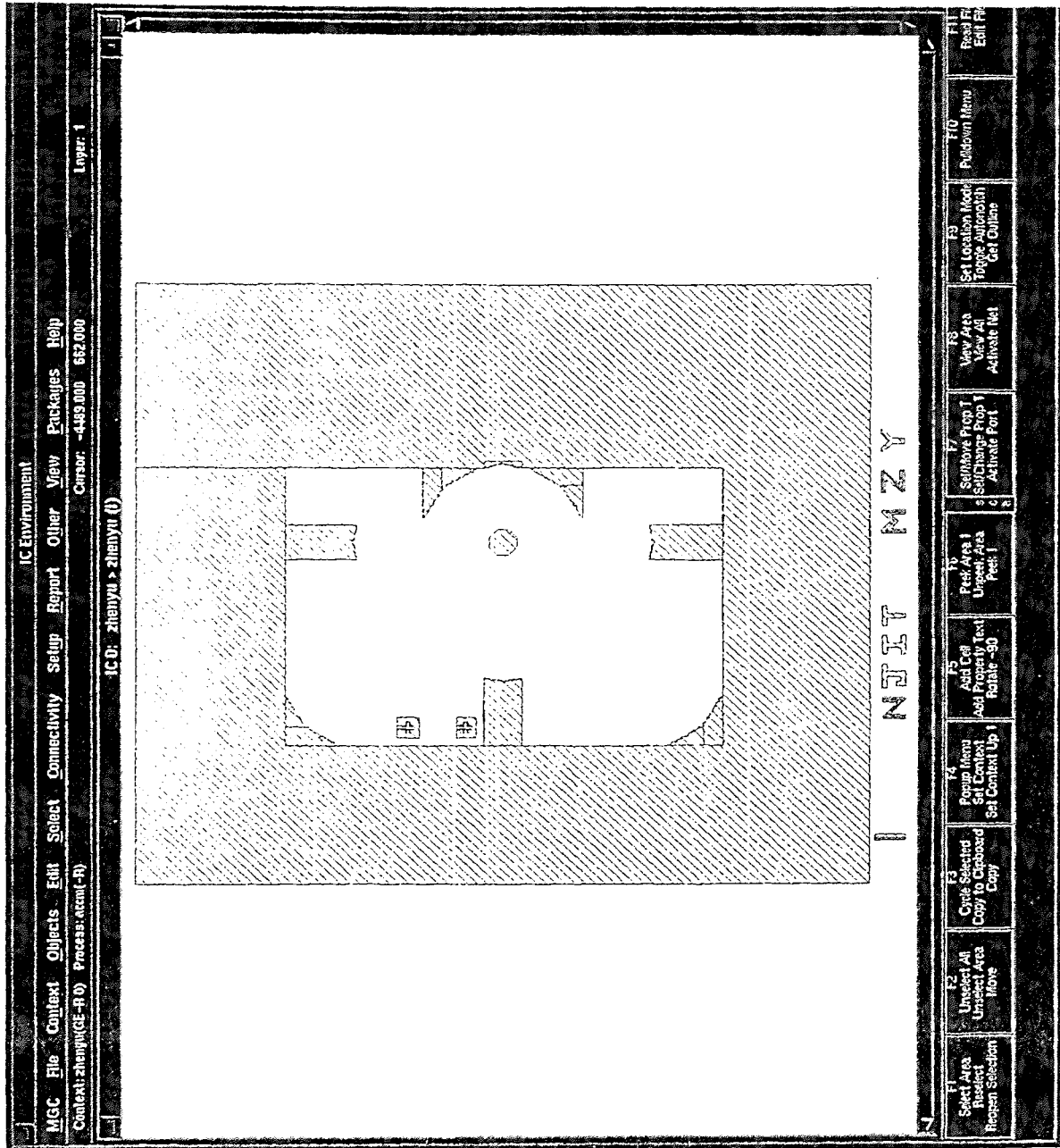
Figure A.2 Top view of the etching hole

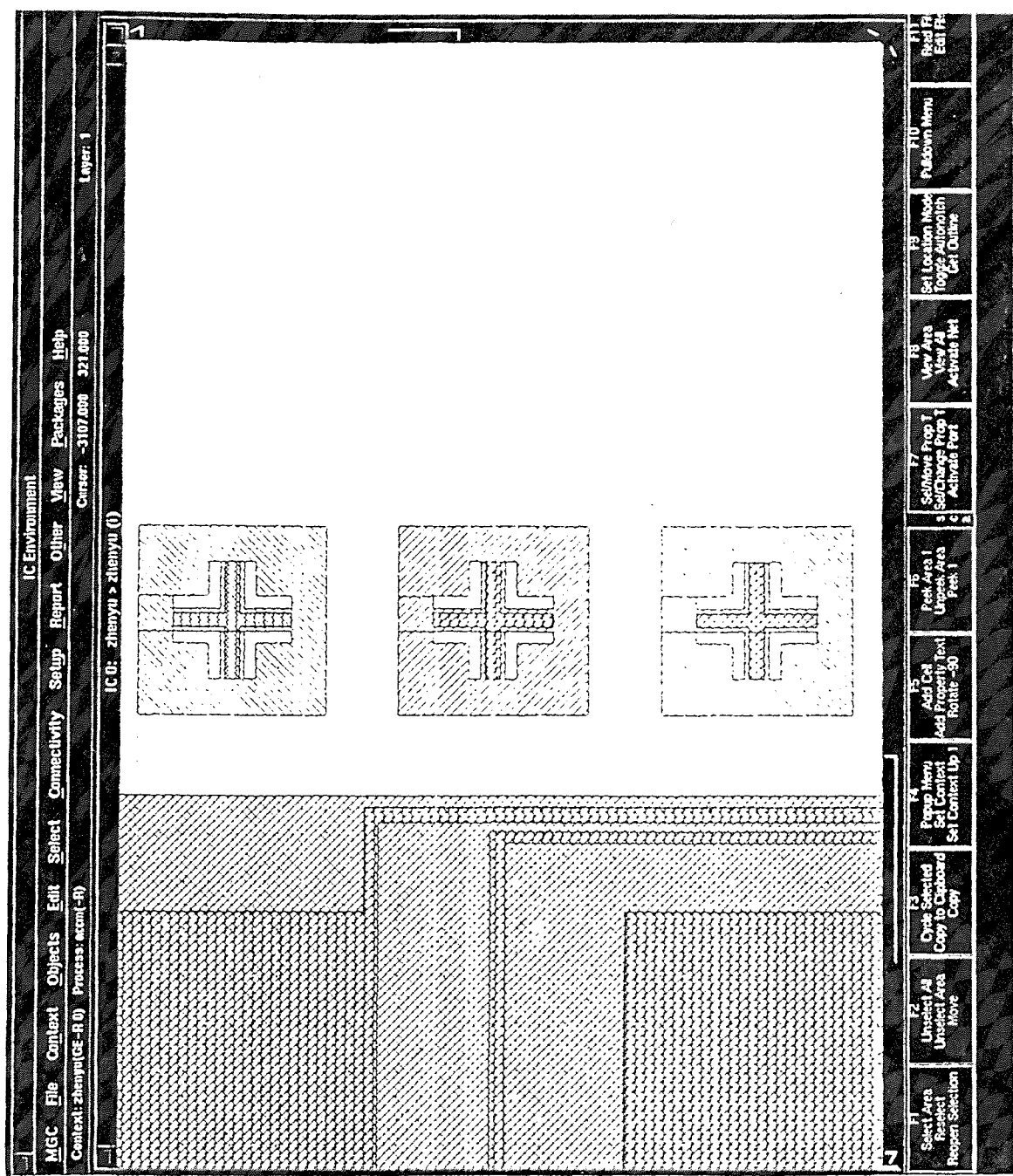**Figure A.3** Top view of the oxidation layer
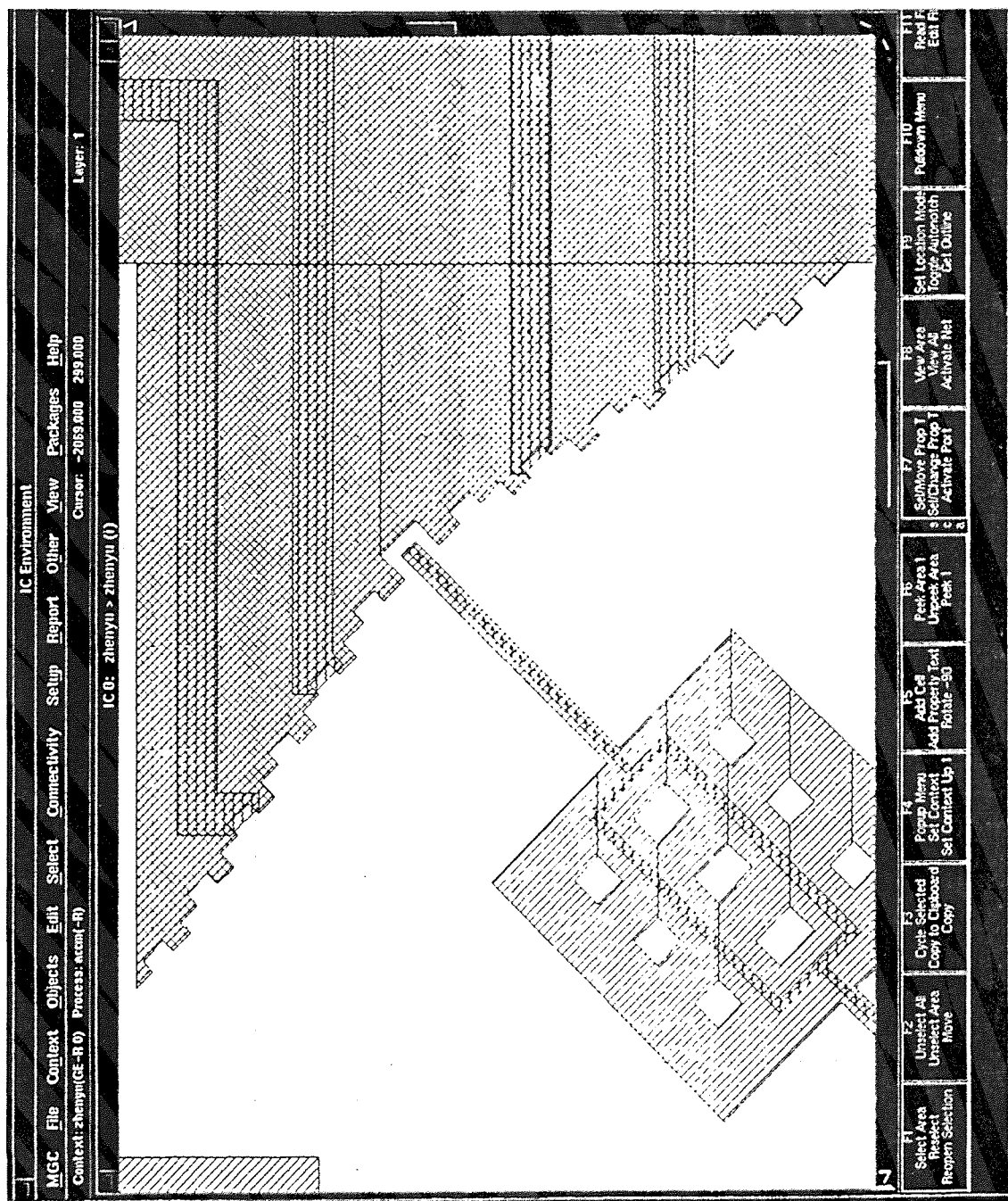
Figure A.4 Top view of the alignment mark

Figure A.5 Top view of the friction tether

APPENDIX B

DERIVATION REFERENCE OF CANTILEVER DEFLECTION

From the equation for the deflection of the cantilever beam (Equation B.1)

$$EI\frac{d\theta}{ds}=P(L-x)=M \tag{B.1}$$

get

$$\frac{d^2\theta}{ds^2} = -\frac{P}{EI}\frac{dx}{ds} = -\frac{P}{EI}\cos\theta \tag{B.2}$$

Integral Equation B.2 get

$$\frac{1}{2}(\frac{d\theta}{ds})^2 = -\frac{P}{EI}\sin\theta + C \tag{B.3}$$

The constant C can be evaluated directly by observing that the curvature at the loaded end is zero. If θ_0 is the corresponding angle of slope

$$\frac{d\theta}{ds} = \sqrt{\frac{2P}{EI}}(\sin\theta_0 - \sin\theta)^{\frac{1}{2}} \tag{B.4}$$

The value of θ_0 cannot be found directly from this equation but it is implied by the requirement that the beam be inextensible, so that

$$\sqrt{\frac{2P}{EI}} \int_0^L ds = \int_0^{\theta_0} (\sin\theta_0 - \sin\theta)^{-\frac{1}{2}} d\theta = \sqrt{2} \left(\frac{PL^2}{EI}\right)^{1/2} \tag{B.5}$$

In order to evaluate this elliptic integral, denote PL^2/EI by α^2 and let

$$1 + \sin\theta = 2k^2 \sin^2\phi = (1 + \sin\theta) \sin^2\phi \tag{B.6}$$

Then we have a classic elliptical integral of the first kind

$$\alpha = \int_{\phi_1}^{\pi/2} (1 - k^2 \sin^2\phi)^{-1/2} d\phi,$$

$$= F(k) - F(k, \phi_1) \tag{B.7}$$

Where $\sin\phi_1 = \dfrac{\sqrt{2}K}{2}$.

so $\quad F(k) - F(k, \phi_1) = \sqrt{\dfrac{PL^2}{EI}}$ $\tag{B.8}$

THE RELATIONSHIP OF THE PROPERTY OF THE CANTILEVER BEAM AND ACCELERATION

The linear relationship between stress and strain for cantilever beam can be expressed by the simple equation

$$\sigma = E*\varepsilon \qquad \text{(C.1)}$$

and from Equation 2.4,2.5 we get

$$\sigma = M*b/(2*I) \qquad \text{(C.2)}$$

Where M is the bending moment, $M=P*L=m*a*L$, a is acceleration, m is the mass on the cantilever beam, L is the length of the cantilever beam. b is the thickness of the cantilever beam, I is the moment of inertia, the relations between stress, strain and acceleration are shown in Figure C.1, C.2.
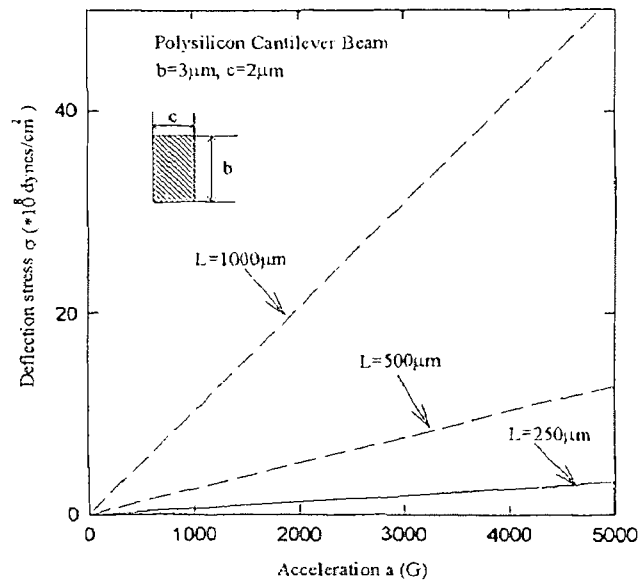

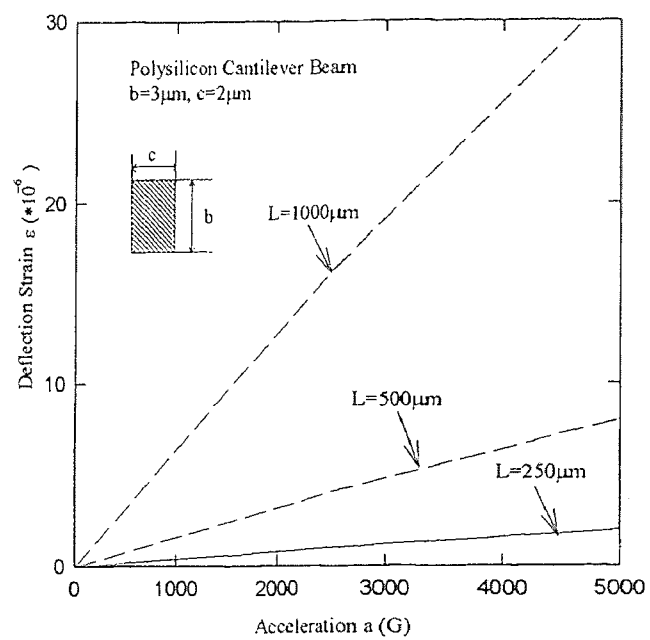**Figure C.1** The relationship between the deflection stress σ and acceleration a

Figure C.2 The relationship between the deflection strain ε and acceleration a

REFERENCES

[1] L. M. Roylance and J. B. Angell, "A batch fabricated silicon accelerometer," *IEEE Trans. Electron Devices*, ED-26, pp.1911-1917, 1979.

[2] M. Nakamura, K. Murakami, H. Nojiri and T. Tominaga, "Novel electrochemical micromachining and its application for semiconductor accelerometer sensor IC," *Tech. Digest, 4th Int. Conf. Solid-State Sensors and Actuators (Transducers'87)*, pp.112-115, 1987.

[3] V. M. McNeil, M. J. Novack and M. A. Schmidt, "Design and fabrication of thin-film micro accelerometers using wafer bonding," *The 7th International Conference on Solid-State Sensors and Actuators*, pp.822, 1993.

[4] P. Barth, F. Pourahmadi, R. Mayer, J. Poydock, and K. Petersen, "A monolithic silicon accelerometer with integral air damping and overrange protection," *Technical Digest, IEEE Solid-State Sensor and Actuator Workshop*, pp.35-38, 1988.

[5] S. Terry, "A miniature silicon accelerometer with built-in damping," *Technical Digest, IEEE Solid-State Sensor and Actuator Workshop*, pp.114-116, 1988.

[6] J. C. Cole, "A new sense element technology for accelerometer subsystems," *Digest of Technical Papers, The 6th International Conference on Solid-State Sensors and Actuators*, pp.93-96, 1991.

[7] R. S. Payne and K. A. Dinsmore, "Surface micromachined accelerometer: a technology update," *Sensor and Actuators*, pp.127-135, February 1991.

[8] W. Yun, R. Howe, and P. Gray, "Surface micromachined, digitally force-balanced accelerometer with integrated CMOS detection circuitry," *Technical Digest, IEEE Solid-State Sensor and Actuator Workshop*, pp.126-131, June 1992.

[9] L. Ristic, R. Gutteridge, B. Dunn, D. Mietus, and P. Bennett, "Surface micro machined polysilicon accelerometer," *Technical Digest, IEEE Solid-State Sensor and Actuator Workshop*, pp.118-121, June 1992.

[10] S. Cho, K. Najafi, and K. D. Wise, "Scaling and dielectric stress compensation of ultra sensitive boron-doped silicon micro structures," *Proceedings of the IEEE MEMS Workshop*, pp.50-55, February 1990.

[11] M. J. Novack, *Design and Fabrication of a Thin-Film Micromachined Accelerometer* Master's Thesis, MIT, Cambridge, MA, September 1992.

58

[12] F. Rudolf, "A micromechanical capacitive accelerometer with a two-point inertial- mass suspension," *Sensors and Actuators*, pp.191-198, 1983.

[13] R. Dell'Acqua, "A bright future for thick film sensors," *SAE Conf. 1989*, February 27-March 2 ,1982

[14] P. Kaufman, "Force balance accelerometer for cost-sensitive application," *Sensors*, pp.19-21, 1988.

[15] D. W. Satchell and J. C. Greenwood, "A thermally-excited silicon accelerometer," *Sensors and Actuators*, pp.241-245, 1989.

[16] D. R. Ciarlo, "A latching accelerometer fabricated by the anisotropic etching of (1110) oriented silicon wafers," *J. of Micromechanics and Microengineering*, pp.10-13, March 1992.

[17] H. Guckel, D. W.Burns, H. A. C.Tilmens, D. W. Deroo, and C. R. Rutigliano, "Mechanical properties of fine grained polysilicon-the repeatability issue," *Technical Digest, 1988 Solid-State Sensor and Actuator Workshop*, pp.96-99, June 6-9, 1988.

[18] W. P. Mason, *Crystal Physics of Interaction Process*, New York Academic Press, 1986.

[19] J. J. Wortman and R. A. Evans, "Young's modulus, shear modulus, and poisson's ratio in silicon and germanium," *J. Appl. Phys.*, Vol 36, No.1, pp.153-156, January 1965.

[20] S. P. Timoshenko, *Mechanics of Materials*, Van nostrand Reinhold Company, New York, 1972.

[21] R. F. Fay, *Flexible Bars*, Butterworth and Co., Ltd., pp.220, 1962.

[22] K. E. Bishop, and D. C. Drucker, "Large deflections of cantilever beams," *Quarterly of Applied Mathematics*, vol. 3, pp.272-275, 1945.

[23] H. J. Barten, "On the deflection of a cantilever beam," *Quarterly of Applied Mathematics*, Vol. 2, pp.168-171, 1944.

[24] F. V. Rohde, "Large deflections of a cantilever beam with uniformly distributed load," *Quarterly of Applied Mathematics*, Vol. 11, pp.337-338, 1953.

[25] H. B. Dwight, *Tables of Integrals and Other Mathematical Data*, The Macmillan Company, New York, 1955.

[26] T. I. Kamins, "Deformation occurring during the deposition of polycrystalline-silicon films," *J. Electrochem. Soc.*, Vol 121, pp.681-684, 1974.

[27] T. Suzuki, "The deformation of polycrystalline-silicon deposited on oxide-covered single crystal silicon substrates," *J. Electrochem. Soc.*, Vol 124, pp.1776-1780, 1977.

[28] D. L. Schilling, C. Belove, *Electronic Circuits: Discrete and Integrated*, McGraw-Hill Company, New York, pp.151-184, 1972.